CHAPTER

31

Mass Production of Sensors Grown by Molecular Beam Epitaxy

Ichiro Shibasaki[1] *and Naohiro Kuze*[2]

[1]Toyohashi University of Technology, Toyohashi, Japan [2]Asahi Kasei Microdevices Corporation, Shizuoka, Japan

31.1 INTRODUCTION

Molecular beam epitaxy (MBE) technology is now widely used for growth of single-crystal thin films, quantum wells, superlattices, and similar structures. The MBE system was developed first as a research system for preparation of single-crystal thin films and superlattices (Cho and Arthur, 1972). Soon, many people wanted MBE systems for production of electronic and optical devices and some kinds of sensors. By using the production MBE system, mass production of compound semiconductor thin films could be performed under the completely closed process without the influence on environment. However, it was not so easy to work to realize such production MBE systems. MBE is thought to be one of the most promising and powerful thin-film growth technologies used for growing single-crystal thin films, quantum wells or superlattices, and so on made mainly from III−V compound semiconductors.

Thin films of narrow-gap materials such as InSb, InAs, and related compound semiconductors were easily grown by MBE and showed high electron mobility. Therefore, the MBE systems have been used for production of electronic devices and magnetic sensors for more than 20 years.

In this chapter, production technologies of narrow-gap III−V semiconductor thin films made from InSb, InAs and related materials grown by MBE, and sensor applications are discussed. The applications to high-sensitivity magnetic sensors such as InSb thin-film Hall elements and InSb thin-film magnetoresistors are demonstrated.

Moreover, in the last section of this chapter, the application to infrared sensors of narrow-bandgap materials grown by MBE is discussed. Although the mid-infrared sensors operating at room temperature without a cooling system have been required for a long time, it was very difficult to realize. However, we have succeeded in developing uncooled InSb photovoltaic infrared sensors operating at room temperature. In this chapter, the MBE growth and device fabrication of p−i−n-based InSb photovoltaic infrared sensors are described. Then the device performance of InSb photovoltaic infrared sensors at room temperature and their application to temperature measurements are demonstrated.

31.2 MASS PRODUCTION OF INSB THIN FILMS BY VACUUM DEPOSITION AND THEIR APPLICATION TO HALL ELEMENTS

An InSb Hall element is a magnetic sensor, which was used first as a magnetic field measurement probe. The Hall element had several kinds of names such as Hall plate, Hall generator, Hall sensor, or Hall element. At first, the InSb Hall elements were made from thin single-crystal InSb (Kataoka, 1965; Wiess, 1969). At that time, the single-crystal Hall element as a magnetic sensor was expensive and could not make a suitable structure for mass production and did not have sufficient reliability as a practical electronic device.

K.G. Gunter proposed (Guenther, 1958a,b) a method named three temperature method to fabricate InSb thin films by vacuum deposition where three temperatures of In source, Sb source, and substrate are operated independently so as to obtain stoichiometric InSb thin film. This method was similar to the MBE process. Soon, Sakai and Ohshita (1960) studied how to fabricate InSb thin-film Hall elements by vacuum deposition. These proposed methods had problems of In and

Molecular Beam Epitaxy.
DOI: https://doi.org/10.1016/B978-0-12-812136-8.00033-5

TABLE 31.1 Typical Properties of InSb Thin Film Formed by Vacuum Deposition (at 25°C)

	Dopant	Electron mobility, μ_H	Electron density, n	Thickness, t
InSb	None	20,000–30,000 $cm^2\ V^{-1}\ s^{-1}$	$2 \times 10^{16}\ cm^{-3}$	0.8 μm

Sb composition or stoichiometry and thickness uniformity for mass production. The vacuum deposition method proposed by K.G. Gunter was ideally good for a very small-scale process or an experimental technique but not adequate for low-cost mass-production technology of InSb thin films.

In the early 1970s, the personal computer and the home-use VCR and many kinds of electronic and information-processing equipment were on the way to development for practical use. These electronic devices required very small-size actuators or DC brushless motors. By use of the Hall element as a magnetic sensor for fine rotation control of the permanent magnet rotor, a very small-size DC brushless motor could be fabricated. Thus, this was a reason that the DC brushless motor was generally called the Hall motor and that the Hall elements, with high magnetic field sensitivity, very small-size practical reliability, or long-time stability and low-cost mass production, were strongly required. However, at the time, there was no InSb Hall element to satisfy such requirements.

An important method for mass production of polycrystalline InSb thin films was developed by a very small group at Asahi Chemical Industry Company Limited (now Asahi Kasei Corporation) at the end of 1970s. This vacuum deposition process may show us a typical concept of thin-film production required from thin-film magnetic sensors and also an insight into production MBE system design (Shibasaki, 1984, 1988, 1989). This method opened the way to the mass production of InSb thin films that were good for fabricating InSb Hall elements. Before discussing MBE, it may be useful to show the concept of the vacuum deposition and the vacuum deposition system for mass production of InSb thin-film Hall elements.

31.2.1 Mass Production of High-Electron-Mobility InSb Thin Films by Multisource Vacuum Deposition Method With Programmed Substrate Temperature Control

The vacuum deposition method was developed, where a specially designed production vacuum deposition system having multievaporation sources and substrate heater was used. This technology was named multisource vacuum deposition method with operation of the programmed substrate temperature control. In the method, using InSb as a source material, the specially programmed source temperatures and programmed time-dependent substrate heating were combined to grow stoichiometric InSb thin films on heated thin mica substrates (Shibasaki, 1984, 1988, 1989, 2000). In this vacuum deposition method, the stoichiometry of InSb thin films is controlled by sequential evaporation of InSb from several source boats. Thus, InSb polycrystal thin films having a high electron mobility of 20,000–30,000 $cm^2\ V^{-1}\ s^{-1}$ and a thickness of 0.8 μm were grown on thin mica substrates and stably mass produced. The crystal growth process may be similar to MBE. The surface of thin mica substrate is perfectly flat and stable under heating. Typical transport properties of the InSb thin films are shown in Table 31.1.

In Fig. 31.1, the temperature dependences of (A) electron mobility, (B) Hall coefficient, and (C) resistivity of the mass-produced InSb thin films are shown.

For the InSb thin films formed by vacuum deposition, we found some new important magneto-transport properties. The electron mobility is almost constant under the temperature change around room temperature as shown in Fig. 31.1A. The temperature dependences of the Hall coefficients and conductivity showed similar behavior. This is shown in Fig. 31.1B and C. This is a special feature for electronic transport of InSb thin film formed on thin mica substrate or grown heteroepitaxially. High sheet resistance and stable temperature dependence at around room temperature are typical properties of InSb thin films by vacuum deposition, as shown in Fig. 31.1A and C. These properties are based on the small temperature dependence of Hall output voltage and the low-power consumption of the InSb thin-film Hall elements.

31.2.2 Application of the Mass-Production InSb Thin Films to High-Sensitivity Hall Elements

Highly sensitive InSb thin-film Hall elements were developed by using InSb thin films by vacuum deposition on mica substrates. The InSb thin films peeled off from the mica substrates were processed in the mass production line to fabricate high-sensitivity InSb thin-film Hall elements. Fig. 31.2A shows the cross-sectional structure of the high-sensitivity InSb thin-film Hall elements, where InSb thin film formed as a Hall element is inserted or/and sandwiched between a ferrite substrate and ferrite chip. By this sandwich structure, magnetic field sensitivity of the Hall element is

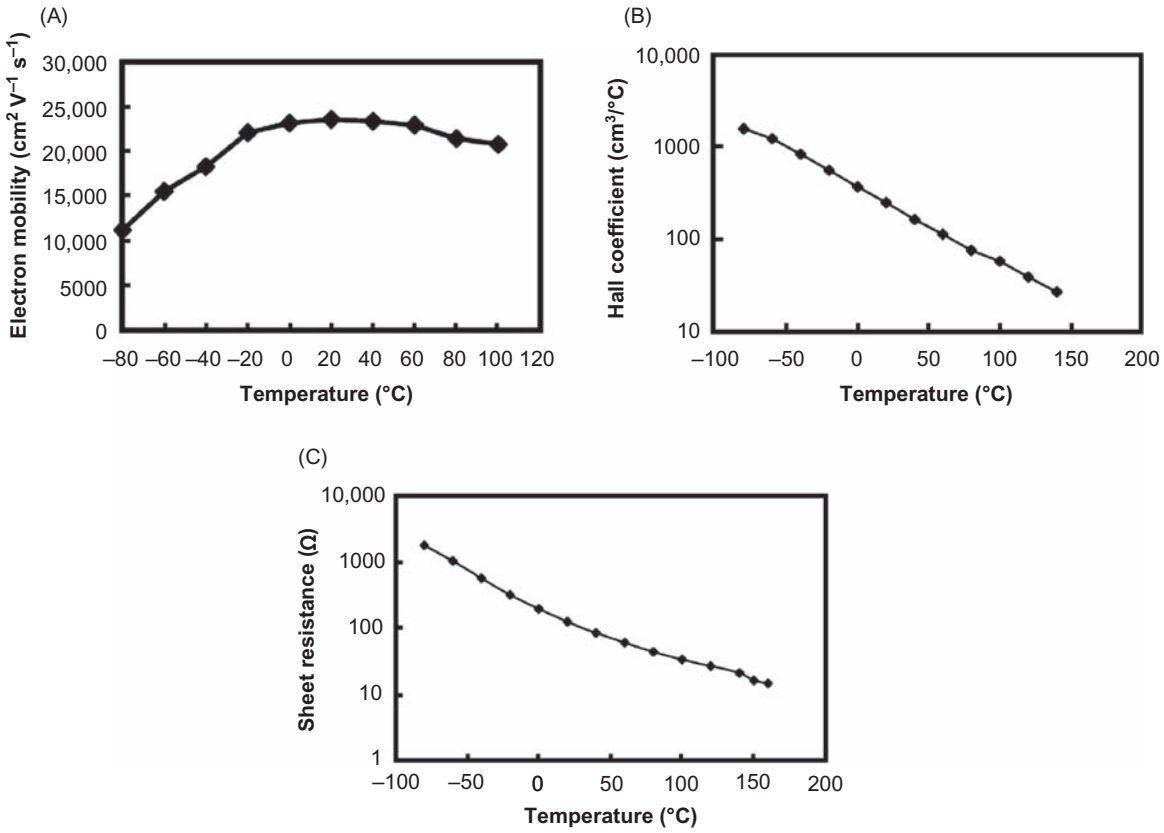

FIGURE 31.1 Temperature dependence of InSb thin film of 0.8 μm thickness, (A) electron mobility, (B) Hall coefficient, and (C) sheet resistance.

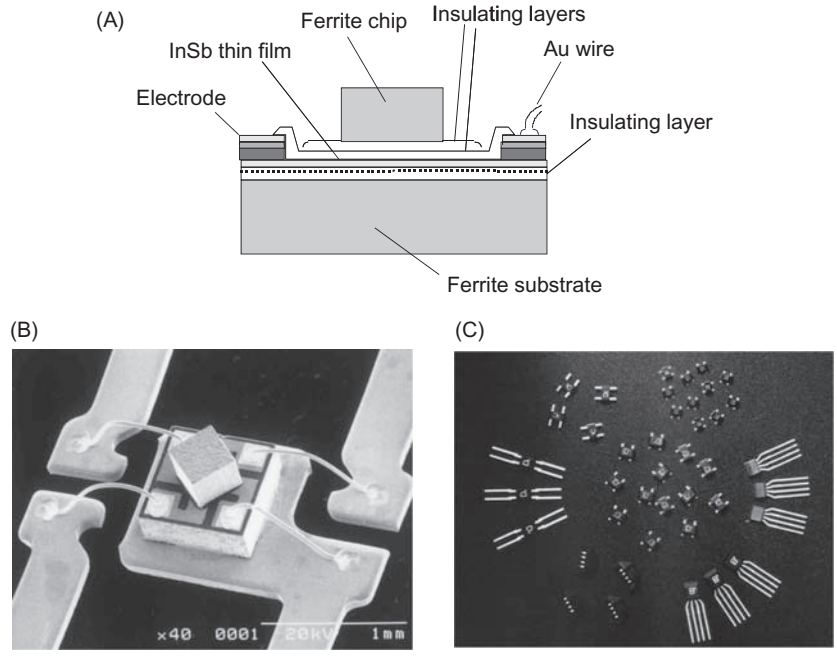

FIGURE 31.2 (A) Cross section of high-sensitivity InSb thin-film Hall element, (B) photograph of the bare chip, and (C) commercial products of InSb Hall elements.

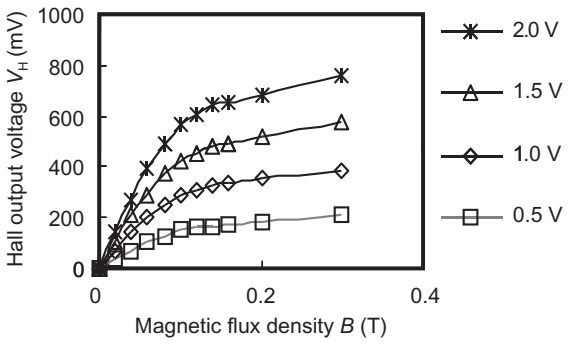

FIGURE 31.3 Magnetic field properties of the high-sensitivity InSb thin-film Hall elements.

amplified about three–six times compared to the original sensitivity obtained from the InSb thin film. Thus, the highest-sensitivity InSb thin-film Hall elements could be realized. The photographs of the InSb thin-film Hall elements are shown in Fig. 31.2. Fig. 31.2B is the bare chip and (C) is their commercial products. Fig. 31.3 shows magnetic field properties of the high-sensitivity InSb thin-film Hall elements for various operation voltages.

This Hall element was completely responsible as the magnetic sensors of small-sized, high sensitivity to detect magnetic flux density and highly reliable for practical electronic parts. The InSb thin-film Hall elements as magnetic sensors have been used to fabricate small-size contactless sensors, switches, and many kinds of contact sensing devices. After the development of the InSb thin-film Hall elements in 1982, more than 20 billion Hall elements have been produced, where the main application was the sensors for DC brushless motors or Hall motors. This large amount of production showed that the vacuum deposition is effective for mass production of electronic parts made from compound semiconductor thin films (Shibasaki, 1995, 2000).

31.3 PRODUCTION MBE SYSTEM FOR INAS HALL ELEMENTS

After the development of the InSb thin-film Hall elements, some of the new applications such as power electronic equipment or current sensor for inverters operating power motors and similar applications required more high reliability and more wide operating range, i.e., an operating range extending from low temperatures far below 0°C to high temperatures far above 100°C. For example, Hall elements used for automotive sensors in the engine compartment require a stable operation at 150°C.

The InSb thin-film Hall elements had a very large temperature coefficient of input resistance of −1.9%/deg caused by the narrow energy gap of InSb. This large temperature dependence of resistance may restrict the operating range of InSb Hall elements around room temperature.

InAs has a little larger energy bandgap of 0.36 eV than InSb. Nondoped InAs polycrystal thin films produced on thin mica substrates by using vacuum deposition similar to the MBE process have an electron mobility of 7000–8000 $cm^2\,V^{-1}\,s^{-1}$ and a high sheet resistance of more than 100 $\Omega\,\Upsilon^{-1}$. The first InAs thin-film Hall elements were developed by using this InAs polycrystal thin film on mica substrates, where the InAs Hall element had the same structure shown in Fig. 31.2A and where the InSb thin film was only replaced by the InAs thin film grown on and peeled off from mica substrates. The InAs Hall element showed more stability under the temperature change and therefore was used for a new application as magnetic sensors. However, it was not sufficiently reliable for some of the new applications.

Bulk single-crystal InAs has a high electron mobility of more than 30,000 $cm^2\,V^{-1}\,s^{-1}$. Experimentally, it was confirmed that a 0.5-μm thick InAs thin film, doped with a suitable amount of Si and grown directly on GaAs (100) substrate, showed a high electron mobility of ∼10,000 $cm^2\,V^{-1}\,s^{-1}$. The electron mobility and resistivity of the InAs thin film showed very little temperature dependence over a wide temperature range. Using this InAs thin film, new Hall elements were developed. The InAs Hall elements had about 50% higher magnetic field sensitivity than commercial GaAs Hall elements and a wider operation temperature range than the InSb thin-film Hall elements. The Hall output voltage of this element has good linearity in a magnetic field. Moreover, this Hall element has very low offset drift, high stability for pulse voltage noise, and low $1/f$ noise, all of which are excellent properties as a magnetic sensor. With these beautiful electrical and magnetic field properties, mass production of the Si-doped InAs thin-film Hall elements was strongly expected.

31.3.1 The First Vertical MBE System for Production of InAs Hall Elements

The first home-designed production MBE system with a vertical growth chamber and an air lock chamber was installed in 1982 (Shibasaki, 1989). This MBE system was designed for research and mass production of InAs thin films on mica substrates. The growth chamber had both a water-cooled shroud and a liquid nitrogen shroud at the peripheral of effusion cell of In

and As. The circular shape of about 200 mm diameter rotating substrate holder with seven 2-in. square substrates kept at a horizontal position was operated in the growth chamber. Source to substrate distance was about 500 mm for every source to obtain thickness uniformity of the InAs thin film. Substrate heater had divided two heating parts of center and peripheral parts for uniform substrate heating, which were independently controlled. The stoichiometric composition of the InAs thin films grown on mica substrates was completely controlled by the As_4 pressure by vacuum pressure sensor at the growth chamber wall. The specially programmed substrate heating from low to high temperature (low temperature for the initial deposition stage of a few minutes and high temperature for the later stage) was operated corresponding to InAs thickness. This substrate heating was similar to the case of InSb vacuum deposition process. The thickness was completely defined by In beam intensity and growth time. The suitable substrate temperature for InAs deposition was higher than InSb.

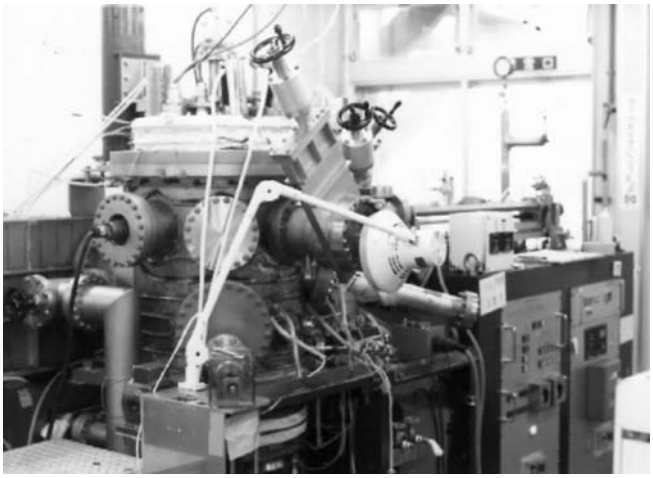

FIGURE 31.4 The first production MBE for InAs thin-film Hall elements installed in 1982. Source: *Courtesy of Asahi Chemical Industry Company Limited.*

A photograph of this first MBE system is shown in Fig. 31.4, which was installed in 1982 for both use in research and production of InAs thin films for Hall element. The first purpose of this MBE system was the growth of InAs polycrystal thin films with high electron mobility on mica substrates. Then the InAs thin films were used for fabricating high-sensitivity InAs Hall elements with the same structure as shown in Fig. 31.2A, which could be operated at higher temperature more than 100°C or a wide operation temperature range and used as a magnetic sensor for a DC brushless motor or a Hall motor.

This MBE also was used experimentally to grow InAs single-crystal thin films on semiinsulating GaAs substrates. The result was not so good. The surface of the InAs thin film was miller but many defects were observed by the microscope. Therefore, detailed growth experiments were not done. The first MBE system was not suitable for single-crystal growth, but the first system gave us many important issues about production MBE system design for large-area crystal growth, as shown in Table 31.2.

31.3.2 Design and Fabrication of the Second Production MBE System

For mass production of single-crystal InAs thin films, we designed and installed a second production MBE system with three chambers and a large growth area or a holder with twelve 2-in. diameter substrates. The most important issue in designing production

TABLE 31.2 Important Issues for Production MBE System

Important issues suggested by 1st MBE	Important comments
(a) Large growth chamber	To Enable keeping higher vacuum
(b) Vertical growth chamber	To make easier to handle large-diameter wafer holder
(c) Large separation/distance between effusion cell and substrates	To minimize the radiation effect of high temperature effusion cell to substrate temperature
(d) Uniform substrate heating over the substrate	Uniform growth and thickness uniformity
(e) Large source capacity (Knudsen cell)	Larger number of growth operations without source material charge
(f) Simple and easy operation	Minimize miss operation
(g) Computer aided automated growth	Minimize miss operation
(h) Easy maintenance and operation safety	Safety for maintenance operators
(i) Small quantity of LN_2 consumption	Low production cost

TABLE 31.3 Design Features of the Production MBE System

1	A large vertical growth chamber with 1100 mm diameter
2	A wafer holder with twelve 2-in. substrates (large growth area)
3	Three thickness uniformity design
	(a) Large separation distance more than 400 mm between substrate position and evaporation sources
	(b) Large off incident angle of molecular beam more than 35° from vertical to substrate folder plane
	(c) Substrate rotation system
4	10 source ports with large-diameter flanges
5	Specially designed Knudsen cells with large capacity (from 100 to 300 cc or more)
6	Stable substrate heating system in growth chamber
7	Entry chamber with 11-wafer holder
8	Substrate holder transfer system employing magnetic coupling
9	Simple and easy automated operation
10	High throughput

MBE systems is the engineering of a mass-production system. For example, easy maintenance is very important in a production system.

Many problems specific to production systems were found by the first system operation. They were considered for the design of the second system. The design features of the production MBE system with three chambers are listed in Table 31.3 (Shibasaki, 1997).

The large-diameter chamber was effective at keeping an ultra-high vacuum during the growth operation by keeping the inner wall surface of the growth chamber at a low temperature under the strong radiation from the substrate heater or/and large-capacity Knudsen cells. Other important points considered in designing the system were low-power consumption in the vacuum chamber for reducing undesired outgassing from the chamber wall and inner housing by heat-up during operation. Reducing thermal interaction between source and substrate each other by radiation was important for temperature stability of sources and substrates. Reducing liquid nitrogen consumption is also very important for low product cost. Uniformity of thin films grown on substrates was affected by a distance between source and substrates (or substrate holder) and an angle between incident beam and vertical line through the center of the rotating substrate holder. The large distance between source and substrate and the large incident beam angle on substrates may produce better uniformity under the restricted space and substrate rotation. The uniformity also might be affected by a distance between the incident beam center and the vertical line on the substrate holder. These three parameters were not independent of each other and optimized to obtain good uniformity for the MBE system. A photograph of the production system is shown in Fig. 31.5. The crystal growth by using this MBE system is discussed in the next section.

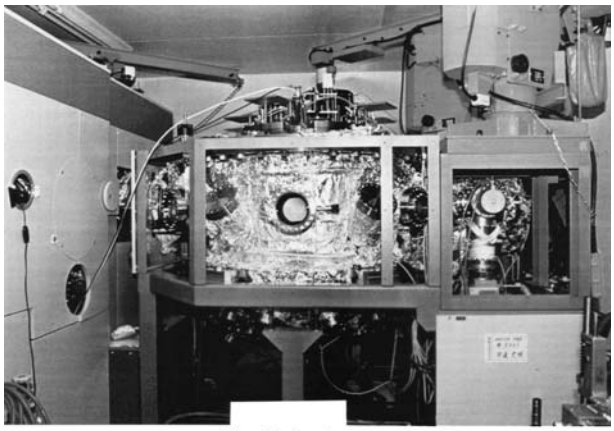

FIGURE 31.5 The first production MBE for InAs thin films. Source: *Courtesy of Asahi Kasei Electronics Limited.*

31.4 LARGE-AREA INAS THIN-FILM GROWTH BY MBE

31.4.1 Mass Production of InAs Single-Crystal Thin Films Grown on GaAs Substrates by the MBE System

The single-crystal InAs thin films on GaAs substrate as shown in Fig. 31.6 were grown by the production

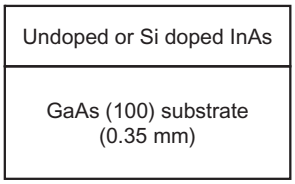

FIGURE 31.6 Cross section of InAs single-crystal thin film on GaAs (100) substrate grown by MBE.

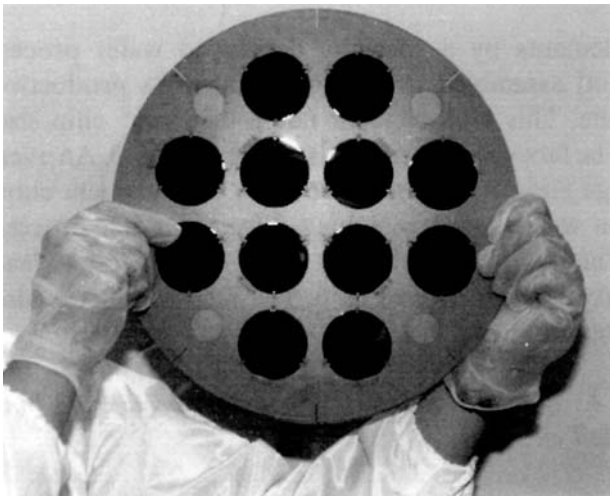

FIGURE 31.7 Substrate holder with twelve 2-in. GaAs substrates of the production MBE system (Shibasaki, 1995).

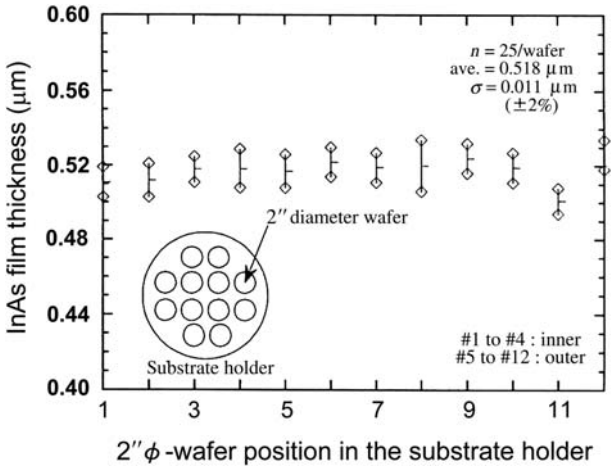

FIGURE 31.8 Uniformity of InAs thin-film thickness grown by the production MBE.

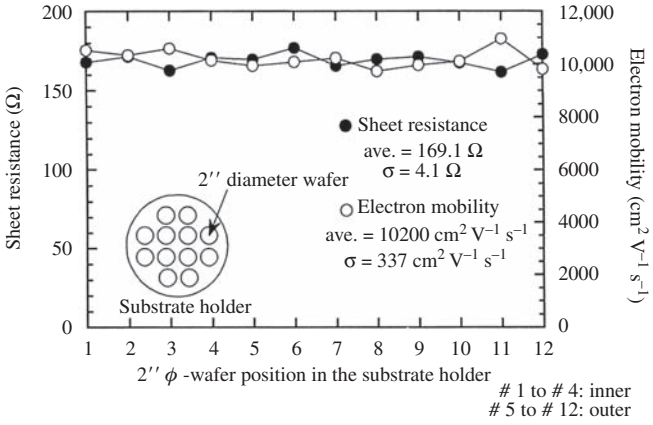

FIGURE 31.9 Uniformity of the electron mobility and sheet resistance of InAs thin films by production MBE (Shibasaki, 1995).

MBE system, with relaxing large lattice mismatch between InAs and GaAs. After long research trials and studies of growth conditions and also many machine problems including the vacuum, heater, and substrate manipulation system, a simple growth condition was found, i.e., the growth condition finally obtained for InAs thin films was simple. The substrate temperature was kept at about 470°C and substrate rotation was around the order of 20 rpm. The In and As cells were operated to keep the constant temperature at an optimized temperature, respectively. All these parameters were experimentally optimized under the condition of growth rate of about 1.0 μm h^{-1} and for obtaining InAs thin films with mirror surface and high electron mobility.

By using this MBE, InAs single-crystal thin films on twelve 2-inch semiinsulating GaAs substrates could be grown under the optimized growth condition. At a constant substrate temperature, InAs single-crystal thin films were grown on semiinsulating GaAs substrates with the large substrate holder, as shown in Fig. 31.7.

31.4.2 Uniformity of InAs Thin Films by Production MBE System

In this section, InAs single-crystal thin films on GaAs substrates grown by the production MBE system are described. There is a well-known large lattice mismatch between InAs and GaAs (about 7%). However, we overcame this large mismatch and found optimized growth conditions for InAs thin films. The growth condition was no different for undoped and Si-doped InAs single-crystal thin films. Uniformity was the most important aspect for the production MBE system. Si-doped InAs thin films of 0.5 μm thickness on GaAs (100) substrate (2° off) without any intermediate buffer layer were grown by the production MBE system. The uniformity of InAs thin film thickness is shown in Fig. 31.8. Uniformity of the electron mobility and sheet resistance of InAs thin films are shown in Fig. 31.9.

The yield of InAs thin films grown by MBE was estimated to be about 95% or more under suitable specifications restricted by device characteristics, i.e., InAs Hall elements. We also experienced good reproducibility with the production the MBE system. However, a small difference in the transport properties between inner position and outer position on the substrate holder was observed, which might be due to the nonuniformity of substrate temperature at both inner and outer positions. With these results, the MBE system was shown to be suitable for mass production, and also it is very useful for production of quantum wells and similar quantum structures.

31.5 TRANSPORT PROPERTIES OF INAS SINGLE-CRYSTAL THIN FILMS AND INAS DEEP QUANTUM WELLS GROWN BY MBE

31.5.1 Transport Properties of InAs Single-Crystal Thin Films Grown on GaAs Substrates

By using the production MBE, we grew Si-doped InAs thin films of 0.5 μm thickness on GaAs (100) substrate (2° off) without an intermediate buffer layer. The typical transport properties are shown in Table 31.4.

The electron mobilities of the undoped InAs thin film and the Si-doped one were compared at room temperature. The electron mobility of Si-doped InAs thin film is larger than the undoped one.

The magneto-transport properties of InAs single-crystal thin films grown by the production MBE were studied for fabrication of InAs Hall elements or Hall sensors for the first time. Temperature dependence of the electron mobility and resistivity of the InAs thin films are shown in Fig. 31.10A and B, respectively.

In Fig. 31.10A and B, we can see the decrease of the temperature dependence by Si doping or it may be n-type impurity doping. This doping effect is useful for realization of the Hall element with high reliability or stability over a wide range of temperature changes. A more detailed comparison of the temperature dependence of the electron mobility with different thicknesses is shown in Fig. 31.11. The doping effect to reduce temperature dependence is apparent around room temperature.

It is important to comment on the effect of Si effusion cell to substrate temperature and the replacement of Si by Sn. There was a little problem to be discussed about the temperature of Si effusion cell, which was a temperature higher than 1100°C. The Si effusion cell produces very strong radiation toward the substrates and thus affects the unwanted substrate temperature change because the substrate temperature suitable for crystal growth of InAs is around 470°C. The Si effusion effect produced a little complexity for the MBE operation. For easy and simple operation of the growth process, n-type impurity Si may be replaced by Sn. By replacing Si with Sn of n-type impurity, the growth condition and the doping effect are not changed. Moreover, Sn effusion cell temperature was lowered to about 400°C. Moreover, the electron mobility of Sn-doped InAs thin films is a little higher than the Si-doped ones. The doping effect did not change by the replacement of Si with Sn. This refers to the universality of the doping effect for any kind of impurity atom (Shibasaki et al., 1991; Iwabuchi et al., 1995).

31.5.2 Fabrication of InAs Deep Quantum Well Grown on GaAs Substrates by Production MBE and Their Transport Properties

31.5.2.1 Fabrication of InAs Deep Quantum Well by Production MBE

InAs has the same zinc-blende crystal lattice structure as GaAs. However, there is a large difference of 6.8% in the lattice constants of InAs and GaAs. Because of this large lattice mismatch, InAs single-crystal thin films grown directly on GaAs substrates by MBE did not have a large electron mobility comparable to the electron mobility of bulk single-crystal InAs.

To eliminate these lattice-mismatch effects, it was found to be effective to grow a buffer layer of $Al_xGa_{1-x}As_ySb_{1-y}$ ($0 < x, y < 1.0$) lattice matched to InAs on a GaAs substrate surface before InAs growth by MBE. In this text, the suffix of x and y is sometimes neglected for simplicity. To obtain a large electron mobility InAs thin layer for magnetic sensor application, the InAs layer sandwiched by the AlGaAsSb buffer and a cap layers is effective (Nagase et al., 1993; Kuze et al., 1995, 1996, 1997; Shibasaki et al., 2005).

TABLE 31.4 Typical Properties of InAs Thin Films Grown on GaAs(001) Surface by MBE

	Dopant	Electron mobility, μ_H	Electron density, n	Thickness, t
InAs	None	9000 $cm^2 V^{-1} s^{-1}$	2.2×10^{16} cm^{-3}	1.2 μm
InAs	Si	10,000 $cm^2 V^{-1} s^{-1}$	7×10^{16} cm^{-3}	0.5 μm

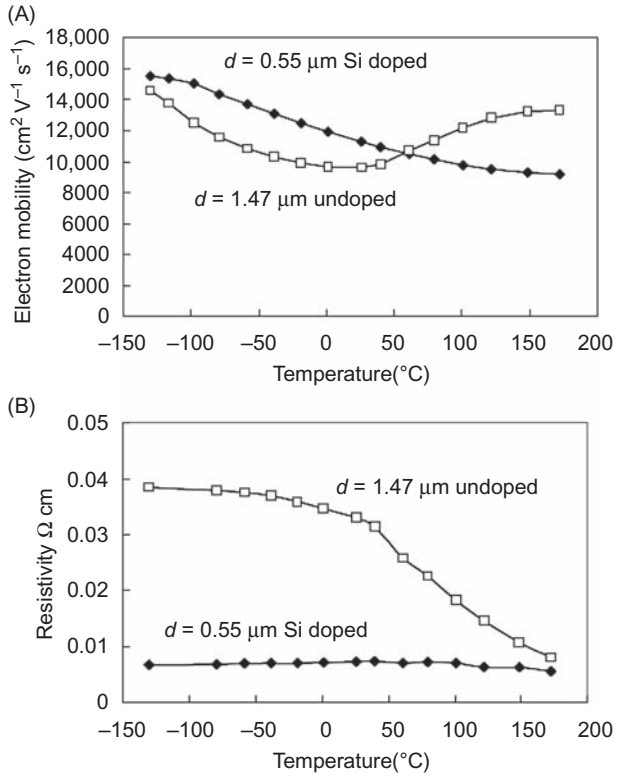

FIGURE 31.10 (A) Temperature dependence of electron mobility and (B) temperature dependence of resistivity of InAs thin films on GaAs (100) substrates by MBE.

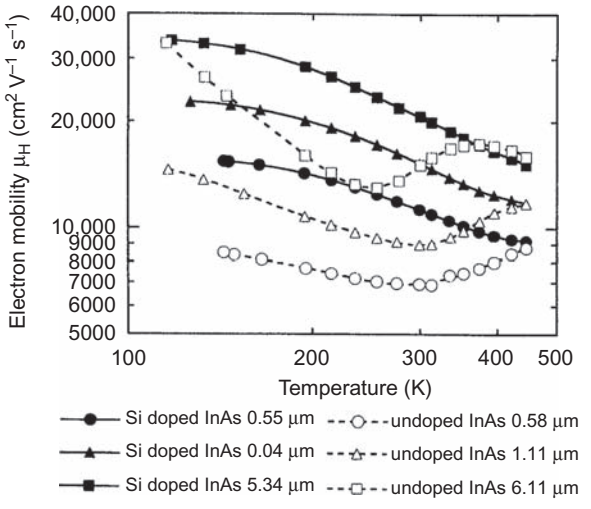

FIGURE 31.11 Temperature dependence of electron mobility of InAs thin films with different thickness on GaAs (100) substrates by MBE.

In the case where a very thin InAs layer was sandwiched by lattice-matched AlGaAsSb layers, an InAs layer formed a quantum well with a very deep potential well, and such a structure is called a deep quantum well (DQW). This InAs DQW shows a very large

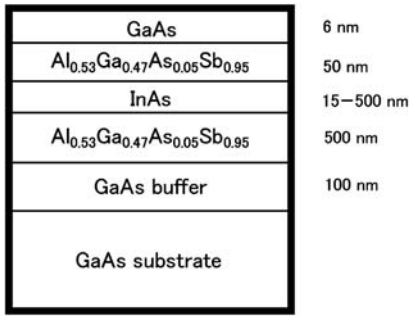

FIGURE 31.12 Cross section of InAs DQW grown on GaAs substrate by MBE (Kuze et al., 1997).

electron mobility and thus is a good material for fabrication of high-sensitivity InAs Hall elements.

We investigated experimentally the growth of the InAs DQW in the case of thicknesses of 15 nm (quantum well) up to 500 nm. Fig. 31.12 shows the sample structure grown by MBE, where an undoped thin InAs layer is sandwiched between AlGaAsSb layers on a GaAs (100) substrate. The AlGaAsSb layers were lattice matched to the InAs. A thin GaAs top layer as a protection layer was also formed on the AlGaAsSb top layer. To obtain the InAs structure sandwiched by AlGaAsSb, a specially designed MBE system equipped with a substrate holder for twelve 2-in. substrates (a production MBE system) was used.

The composition of $Al_xGa_{1-x}As_ySb_{1-y}$ $(0 < x, y < 1.0)$ was fixed to $x = 0.53$ and $y = 0.05$, i.e., $Al_{0.53}Ga_{0.47}As_{0.05}Sb_{0.95}$, and this composition had almost the same lattice constant as InAs; i.e., the lattice mismatch determined by X-ray diffraction measurement was about 0.5%.

A specially developed growth condition was used for growth of the InAs DQW and the InAs structure sandwiched by AlGaAsSb. No impurity doping was done for either InAs or AlGaAsSb. The substrate temperature was kept constant at 470°C for AlGaAsSb, InAs, and GaAs. To prepare the samples, the growth conditions such as beam intensities of In, Ga, As, and Sb were fixed, and only the growth time of InAs was varied corresponding to various InAs thicknesses. For all samples, the growth condition was fixed except for the growth time corresponding to InAs thickness for various samples.

31.5.2.2 *Transport Properties of InAs DQW Grown by MBE*

The most important and basic property of the InAs DQW is the transport property at room temperature and its thickness dependence. In Fig. 31.13A, the thickness dependence of the electron mobility was shown from 15 to 500 nm of InAs quantum well thickness. The electron mobility of InAs DQW increased at InAs

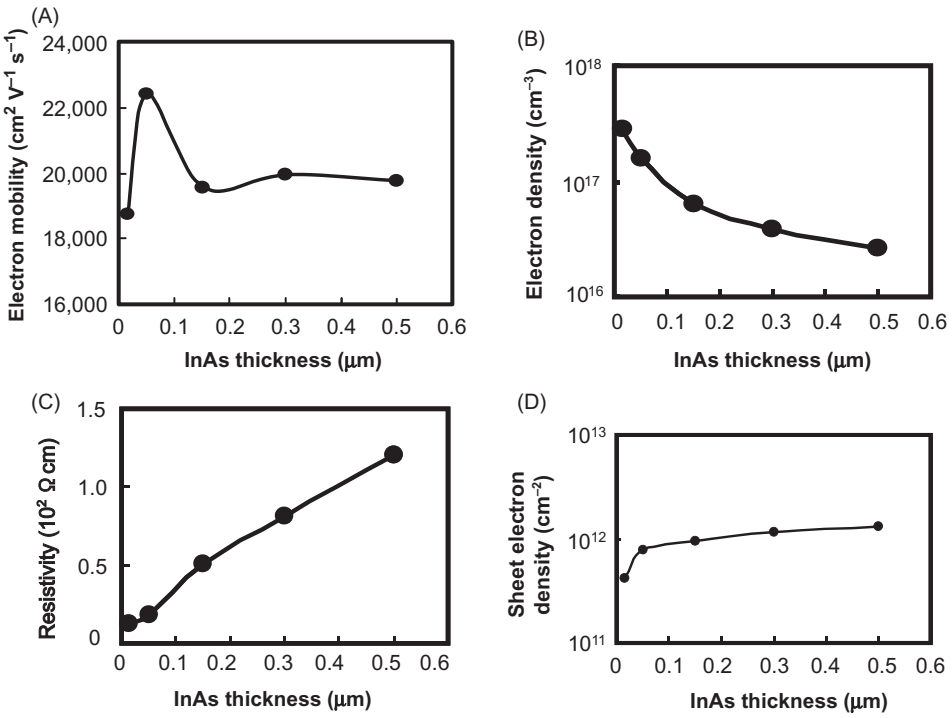

FIGURE 31.13 Thickness dependence of (A) electron mobility, (B) electron density, (C) resistivity, and (D) sheet electron density of the InAs DQW grown by MBE.

thickness less than 100 nm, and it peaked at approximately 50 nm. The electron mobility of the samples with more than 150 nm of InAs thickness was low. In addition, the electron mobility did not increase even if we increased the InAs quantum well thickness. This thickness dependence of the electron mobility shows the existence of a critical thickness for the InAs layer. These results showed that the electron mobility became higher within a critical thickness of InAs and was almost kept constant at a thickness of more than the critical thickness.

Since the 50 nm AlGaAsSb cap layer was not so thick, the 6-nm GaAs cap layer may affect the crystal quality of the InAs layer. This effect may be the largest for the 15-nm-thick sample and the electron mobility of the 15-nm-thick sample was the smallest in the all samples. Fig. 31.13B shows the thickness dependence of electron density at room temperature. The conduction electron in the InAs layer may be a sum of the intrinsic electrons and the fixed number of electrons with almost no thickness dependence. The number of the intrinsic electrons in the InAs layer has thickness dependence and may be increased with increasing InAs thickness. However, the electron density is the highest for the 15-nm sample among the all samples and decreases with increasing InAs thickness. This means that the fixed number of conduction electrons in the InAs layer with no thickness dependence may be not so small. Fig. 31.13C shows the thickness dependence of resistivity at room temperature. The resistivity increases monotonically. These results may strongly suggest that most of the conduction electrons come from the AlGaAsSb/InAs heterointerface and the contribution of the intrinsic electron is small. This is more apparent from the sheet electron density shown in Fig. 31.13D, where the increase of sheet electron density with InAs thickness is large at less than 50 nm and very small at more than 50 nm.

In Fig. 31.14A, the temperature dependence of the electron mobility is shown for InAs DQW thicknesses from 15 to 500 nm and for InAs directly grown on GaAs (100) with a thickness of 500 nm for comparison.

In Fig. 31.14A, the electron mobilities for all thicknesses of InAs sandwiched by AlGaAsSb were larger than that of InAs grown directly on a GaAs substrate. As the InAs QW layers sandwiched by AlGaAsSb were lattice matched to AlGaAsSb, the thin-film quality of InAs QW layers was better than the InAs layer directly grown on GaAs substrate.

The electron mobility is very large at lower temperatures and decreases with increasing temperature for the InAs sandwiched by AlGaAsSb except for the 15-nm-thick InAs. Since the lattice scattering decreases at lower temperatures, the electron mobility increases with decreasing temperature. However, the electron mobility of the 15-nm-thick InAs decreased at a low temperature. In other words, the 15-nm-thick InAs showed a temperature dependence different from the other thick samples. This means that the electron transport in the 15-nm-thick InAs DQW sample may not be dominated by lattice scattering at lower temperatures. Moreover, its crystal quality may be low compared to the other thick InAs

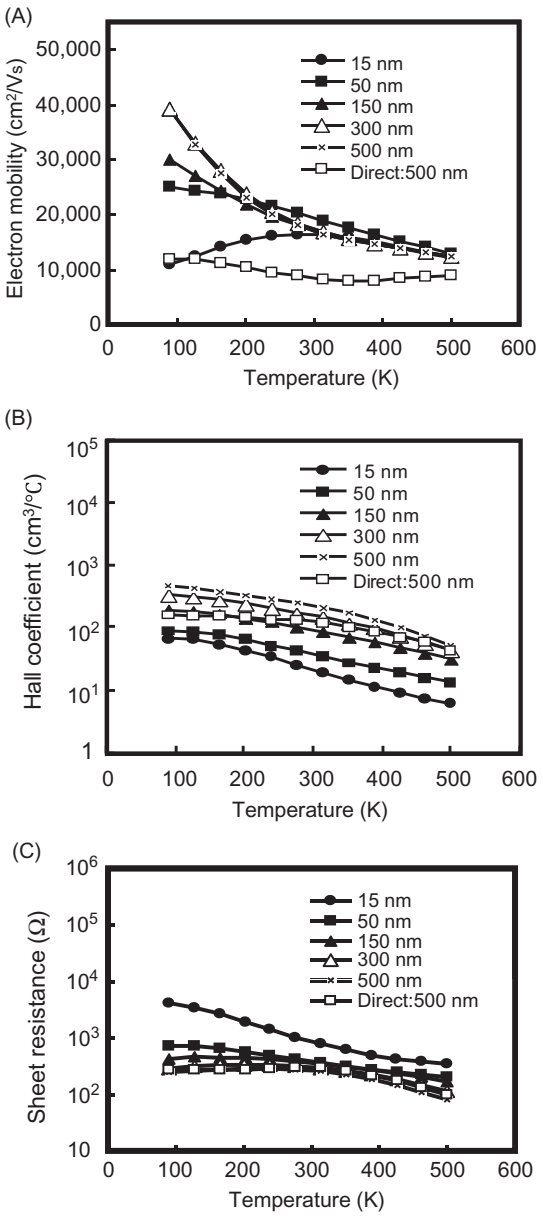

FIGURE 31.14 Temperature dependence of (A) electron mobility, (B) Hall coefficient, and (C) sheet resistance of InAs DQW grown by MBE.

samples. The anomalous temperature dependence and the low value of electron mobility of the 15-nm-thick InAs DQW at a low temperature may therefore be due to the relatively low crystal quality caused by the lattice-mismatch effect of the GaAs top layer. In our experiment, by replacing the GaAs top layer with a large lattice mismatch by GaAsSb lattice matched to InAs, the electron mobility of the 15-nm InAs sample showed a higher electron mobility at a low temperature and no anomalous temperature dependence.

Fig. 31.14B shows the temperature dependence of the Hall coefficient. The Hall coefficient is the lowest for the 15-nm-thick InAs DQW sample, and the 500-nm-thick InAs DQW has the highest value. The temperature dependence of the Hall coefficient monotonically decreases with increasing temperature for all samples. Fig. 31.14C shows the temperature dependence of sheet resistance of the InAs DQW. The variation with temperature is small.

As seen above, InAs DQWs have high electron mobilities, high sheet resistances, and also their temperature dependence is small. These properties are good for fabricating temperature-stable Hall elements, which could be operated at a wide range of temperatures.

31.6 FABRICATION OF INAS SINGLE-CRYSTAL THIN-FILM HALL ELEMENTS AND INAS DQW HALL ELEMENTS

The high electron mobilities of InAs single-crystal thin films and InAs DQWs grown by MBE show a big potential to fabricate high-sensitivity Hall elements as magnetic sensors. By using InAs single-crystal thin films and InAs DQWs, we fabricated high-sensitivity InAs Hall elements and InAs DQW Hall elements, respectively. Temperature dependence of the InAs Hall element is very small compared with InSb thin-film Hall elements. The typical characteristic of InAs Hall elements is stability at a wide range of operation temperatures. In this section, Hall elements made from InAs thin films and InAs DQWs are discussed.

31.6.1 Fabrication of InAs Hall Elements Made From InAs Single-Crystal Thin Film by MBE

Practical InAs Hall elements with 0.36 mm^2 chip size were fabricated by using 0.5-μm-thick Si-doped InAs thin films grown by MBE for the first time. For mass production of the InAs thin-film Hall elements, a specially developed wafer process and assembly process were developed. The fabrication process is shown in Fig. 31.15.

Fig. 31.16A shows a photograph of the InAs Hall element chip made from Si-doped InAs thin film grown on semiinsulating GaAs substrate by MBE, and (B) shows some samples of commercial products. The typical properties of the InAs Hall elements are temperature stability and very good proportionality or linearity to magnetic flux density. Therefore, the first application of this Hall element was a magnetic sensor for direct current sensor.

The magnetic field property is shown in Fig. 31.17 for the Si-doped InAs Hall elements made from InAs single-crystal thin films grown on GaAs substrates by

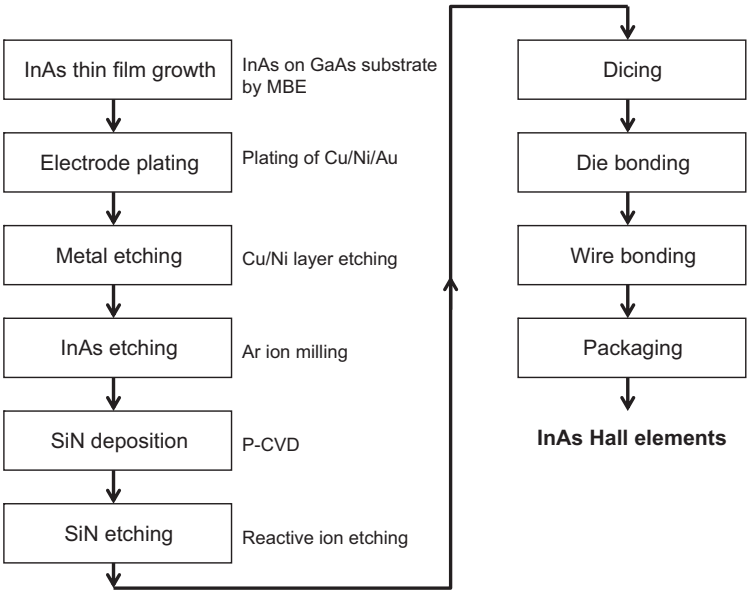

FIGURE 31.15 Typical fabrication process of the InAs Hall elements made from InAs single-crystal thin films grown on GaAs substrates by MBE.

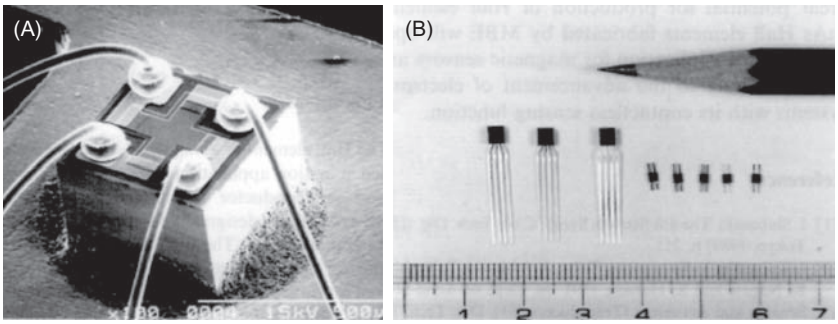

FIGURE 31.16 Photographs of (A) InAs thin film Hall element chip and (B) InAs thin-film Hall elements made from Si-doped InAs single-crystal thin-film grown on GaAs substrate by MBE.

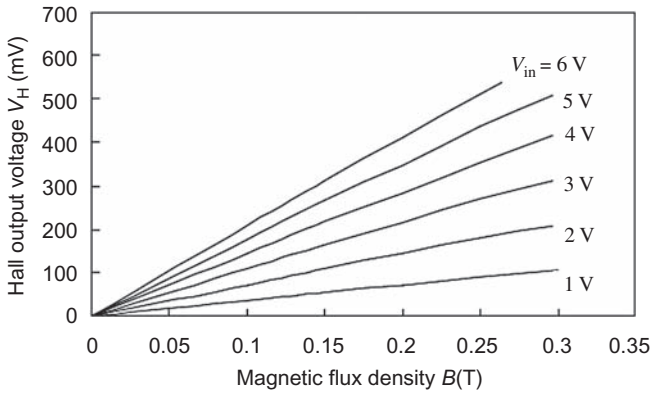

FIGURE 31.17 Magnetic field characteristics of InAs Hall elements made from InAs single-crystal thin films grown on GaAs substrates by MBE (constant voltage operation).

MBE at constant voltage operation. The very good proportionality to detected magnetic flux density is shown in Fig. 31.17.

The temperature dependence of the Hall output voltages for both constant current and constant voltage operations is shown in Fig. 31.18A and B, respectively. The temperature dependence of the InAs Hall elements made from both Si-doped and undoped InAs thin films is compared. It is clear that the Si doping to InAs thin film is effective in reducing the temperature dependence of the Hall output voltage at the constant voltage operation.

The small temperature variation of the input resistance, as shown in Fig. 31.19, is the most important for practical use. It is clear that the Si doping to InAs thin film is effective in reducing the temperature dependence of input resistance at a higher temperature, more than 100°C, of the InAs Hall elements.

31.6.2 Fabrication of InAs DQW Hall Elements Made From InAs DQWs by MBE

InAs DQW Hall elements made from InAs DQW with 50-nm thickness as an active layer have high sensitivity in the magnetic field as a magnetic sensor. Moreover, InAs Hall elements and InAs DQW Hall elements have a very small temperature dependence compared with InSb thin-film Hall elements. The InAs

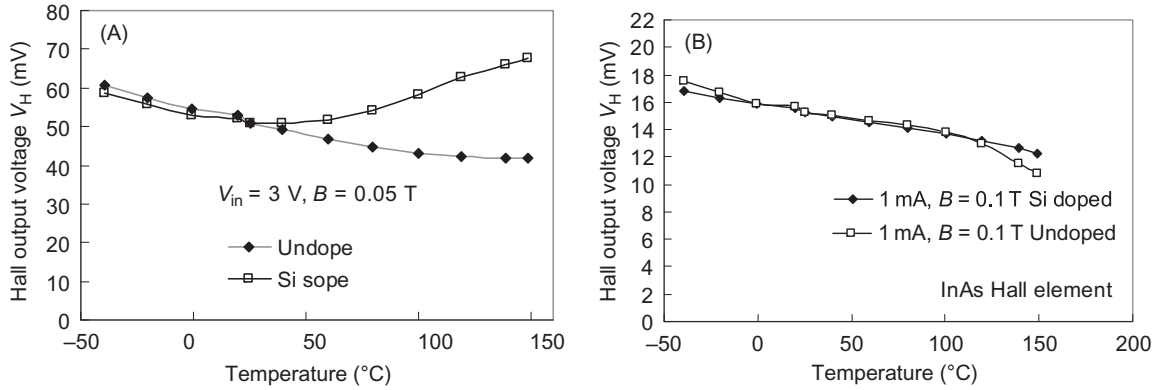

FIGURE 31.18 Temperature dependence of Hall output voltage of InAs Hall elements made from Si-doped InAs single-crystal thin films grown on GaAs substrates by MBE, (A) constant voltage operation and (B) constant current operation.

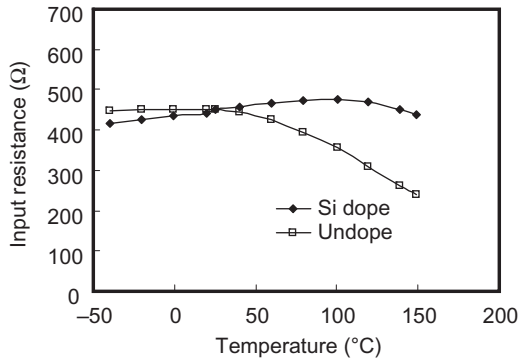

FIGURE 31.19 Temperature dependence of input resistance of InAs Hall elements made from InAs single-crystal thin films grown on GaAs substrates by MBE.

Hall elements are stable at a wide range of ambient temperatures.

The standard specifications of InSb Hall elements amplified by ferrite chips, as shown in Fig. 31.2, InAs Hall elements fabricated from Si-doped InAs and InAs DQW Hall elements are tabulated in Table 31.5.

In Fig. 31.20, photographs are shown of (A) a current sensor with InAs DQW Hall element as a magnetic sensor, where InAs DQW Hall element detects magnetic field produced in a gap of ferrite core by current and (B) inverter for air conditioning system with the InAs DQW current sensors.

31.7 GROWTH OF INSB SINGLE-CRYSTAL THIN FILMS BY MBE AND MAGNETIC SENSOR APPLICATION

InSb has the highest electron mobility and important material for fabrication of high-sensitivity magnetic sensors. Therefore, in this section, the growth of InSb thin films on GaAs substrates and their transport properties, magnetoresistance (MR) effect, and application are discussed.

31.7.1 MBE Growth of InSb Thin Films by Production-Scale MBE System

At first, we review the MBE growth of InSb thin films on GaAs substrates. There is a large lattice mismatch of about 14% between InSb and GaAs. Neglecting the large lattice mismatch, the InSb films with 1.0 μm thickness were directly grown on semi-insulating GaAs (100) substrates. For growth of InSb single-crystal thin films on GaAs substrates, a standard production-scale MBE system (VG100 vertical MBE system with several options) was used, which is shown in Fig. 31.21A the MBE system and (B) substrate holder with twelve 2-in. GaAs substrates.

For the growth of InSb on GaAs semiinsulating substrates, elemental In and Sb_4 were used as source materials, and elemental Si and Sn as n-type doping sources and elemental Ga and As_4 were also used to grow a GaAs buffer layer. After maintaining the GaAs substrate at 650°C for 5 min under As_4 vapor, InSb thin films were grown at the growth rate of 1.0 μm h^{-1} and at the beam flux ratio Sb/In of 10–20 and substrate temperatures between 420 and 460°C. In-situ impurity doping of Si or Sn was done in the InSb layer. This growth condition was first optimized so as to obtain single-crystal InSb thin films with a high electron mobility (Okamoto et al., 2001).

The transport properties of InSb single-crystal thin films at room temperature (300 K) were measured with respect to the MBE growth condition. Fig. 31.22 shows

TABLE 31.5 Typical Characteristics of InSb and InAs Hall Elements

	Film thickness (Active layer) (μm)	Operation voltage, V_{in} (V)	Hall output voltage, V_H ($B = 0.1$ T) (mV)	Offset voltage, V_u ($B = 0$ T) (mV)	Input resistance (Ω)
InSb	0.8	1	200–350	$< \pm 7$	350
InAs	0.5	6	100	$< \pm 16$	350
InAs DQW	0.05	6	250–300	$< \pm 16$	700

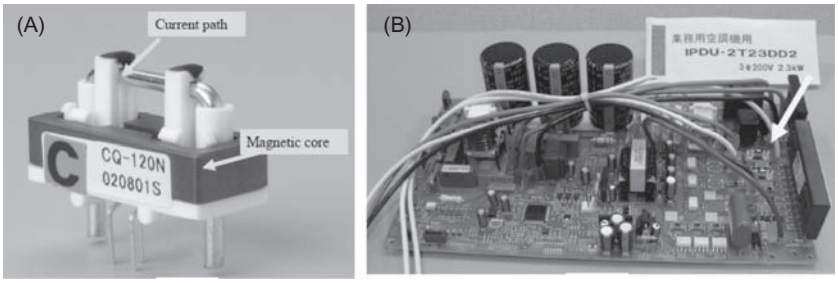

FIGURE 31.20 Photographs of (A) current sensor with InAs DQW Hall element as magnetic sensor and (B) inverter with the current sensors. Source: *Courtesy of (A) Asahi Kasei Electronics and (B) Toshiba Carrier.*

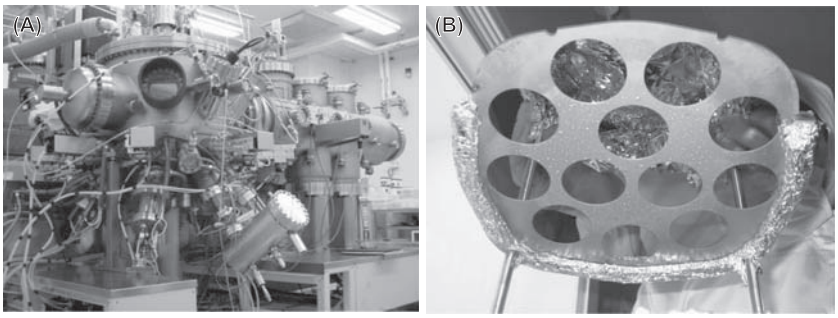

FIGURE 31.21 Photographs of (A) production MBE VG100 system and (B) substrate holder with 12 GaAs substrates.

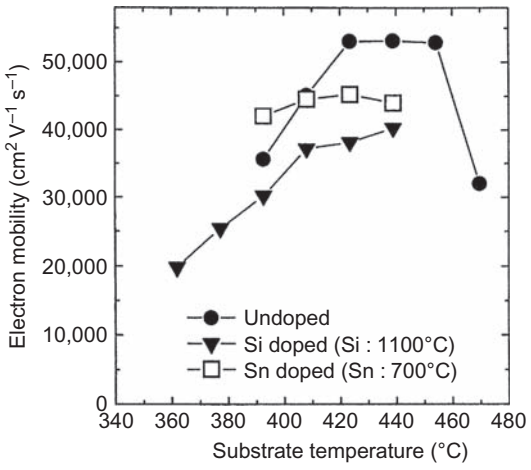

FIGURE 31.22 Substrate temperature dependence of electron mobility of InSb single-crystal InSb thin films with 1.0 μm thickness grown on GaAs by MBE.

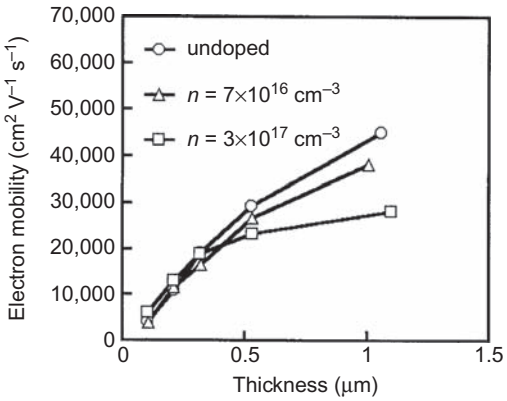

FIGURE 31.23 Thickness dependence of electron mobility of the InSb thin films grown on GaAs by MBE.

substrate temperature dependence of electron mobility of InSb thin films for various cases.

In Fig. 31.23, thickness dependence of the electron mobility is shown. Very large thickness dependence of the electron mobility was observed for various electron densities at room temperature, which may be the effect of the large lattice mismatch of 14% between InSb and GaAs.

This large thickness dependence suggested the existence of a low electron mobility layer near the heterointerface because of the large lattice mismatch at the InSb/GaAs heterointerface (Okamoto and Shibasaki, 2003).

By microscope observation, we could see a smooth and mirror-like InSb surface. In Fig. 31.24A, a photograph of a cross-sectional transmission electron microscopy (TEM) image of InSb and GaAs heterointerface is shown where InSb seven lattice lines and eight lattice lines of GaAs correspond to make periodic two-dimensional superlattices at the heterointerface, and the interface model is shown in Fig. 31.24B. The similar interface was also observed for InAs and GaAs heterointerface where the lattice mismatch is 7%, and InAs 13 lattice lines correspond to GaAs 14 lattice lines.

31.7.2 Electronic Transport Properties of InSb Films Grown by MBE

The typical electron mobility of the undoped InSb thin film with 1.0 μm thickness was 54,000 $cm^2\,V^{-1}\,s^{-1}$, and the electron density was approximately $2\times10^{16}/cm^3$ at room temperature. Fig. 31.25 shows the relationship between electron mobility and electron density (concentration) for undoped, Si-doped, and Sn-doped InSb thin films grown by MBE. The electron mobility of doped InSb films was lower than that of undoped InSb films. The Sn-doped InSb thin films showed a higher electron mobility than Si-doped ones.

In Fig. 31.26, temperature dependence of electron mobility of the InSb single-crystal thin films was plotted. Undoped InSb thin films showed irregular temperature behavior, which was different from the other doped films.

Fig. 31.27 showed temperature dependence of the electron density. The undoped InSb showed different behavior compared to other doped InSb films, and its electron density decreased at low temperature.

Fig. 31.28 shows temperature dependence of resistivity, which is important for the Hall element application. By doping n-type impurity into InSb, the temperature dependence of electronic properties was much reduced. As we mentioned above, the basic

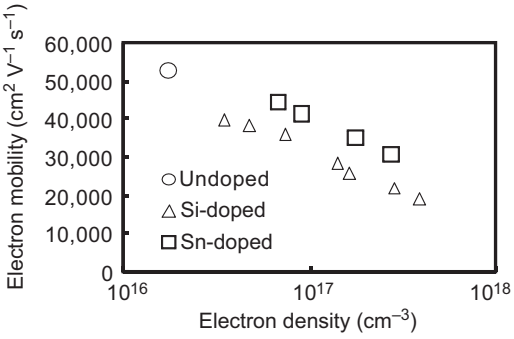

FIGURE 31.25 Relation between electron mobility and electron density for various doping conditions.

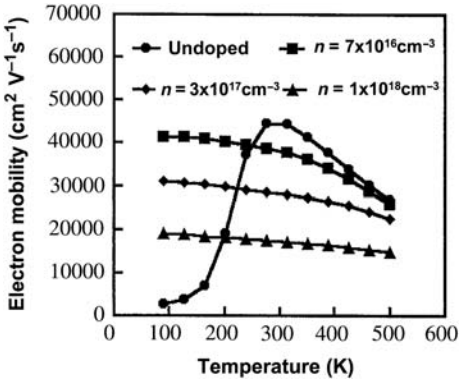

FIGURE 31.26 Temperature dependence of electron mobility of the InSb thin films grown by MBE.

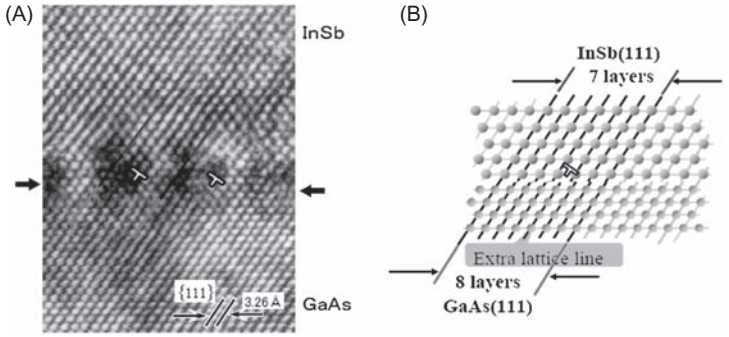

FIGURE 31.24 (A) TEM photograph of the large lattice mismatch boundary between InSb and GaAs and (B) lattice matching model of TEM image.

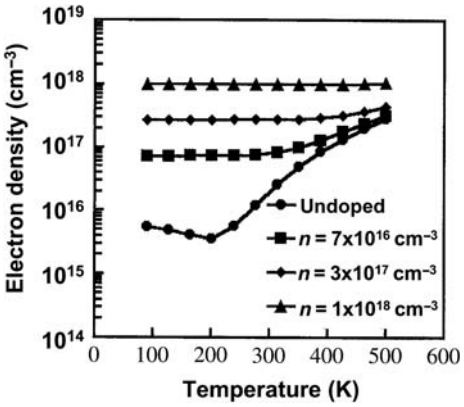

FIGURE 31.27 Temperature dependence of the electron density of InSb thin films grown by MBE.

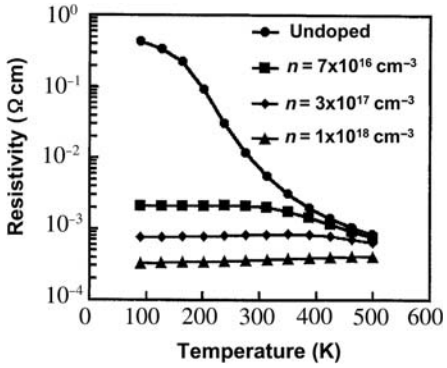

FIGURE 31.28 Temperature dependence of resistivity of InSb thin films grown by MBE.

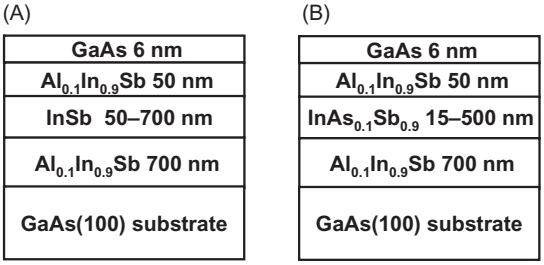

FIGURE 31.29 (A) InSb sandwiched by $Al_{0.1}In_{0.9}Sb$ layers and (B) sandwiched by $Al_{0.1}In_{0.9}Sb$ layers.

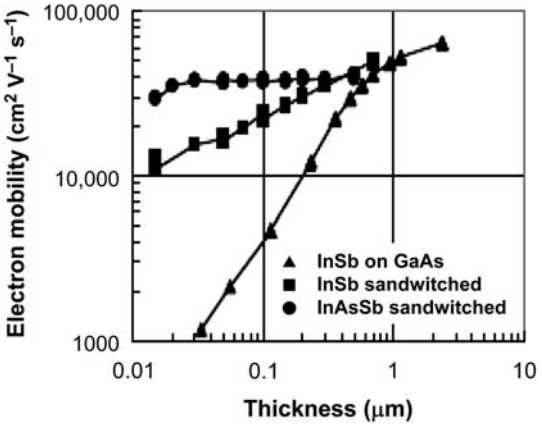

FIGURE 31.30 Thickness dependence of InSb thin films directly grown on GaAs, InSb sandwiched by $Al_{0.1}In_{0.9}Sb$ layers grown on GaAs and $InAs_{0.1}Sb_{0.9}$ sandwiched by $Al_{0.1}In_{0.9}Sb$ layers grown on GaAs.

transport properties of the undoped InSb thin films grown on GaAs substrates showed different temperature dependence compared with other doped ones. This difference was observed for both InSb and InAs single-crystal thin films grown on GaAs substrates, neglecting large lattice mismatch and typical for large lattice-mismatched or metamorphic epitaxy.

31.7.3 Electronic Transport Properties of InSb Thin Films Grown on Reduced Lattice Mismatch Substrate by MBE

In this section, we will discuss the growth of In(As)Sb thin films on an insulating layer of $Al_{0.1}In_{0.9}Sb$ having a lattice mismatch of 0.5% to InSb to reduce the lattice mismatch of 14% between InSb and GaAs. The sample structures shown in Fig. 31.29A and B were grown by MBE and their transport properties were measured. Fig. 31.30 shows the thickness dependence of electron mobility of InSb directly grown on GaAs, InSb sandwiched by $Al_{0.1}In_{0.9}Sb$ layers and $InAs_{0.1}Sb_{0.9}$ sandwiched by $Al_{0.1}In_{0.9}Sb$ layers, which lattice matched to $InAs_{0.1}Sb_{0.9}$. The electron mobility reduced with increasing lattice mismatch values. The effects of the reduction of lattice mismatch for three cases are apparent (Geka et al., 2007; Shibasaki et al., 2009).

31.7.4 Low Temperature Transport Properties and Band Diagrams of InSb and $InAs_xSb_{1-x}$ Quantum Wells Grown by MBE

In the former section 31.7.3, we discussed InSb and $InAs_xSb_{1-x}$ thin layers for $x = 0.1$ grown on reduced lattice mismatch substrates by MBE, which were shown in Fig. 31.29A and B. In Fig. 31.29, InSb and $InAs_xSb_{1-x}$ thin layers sandwiched between $Al_{0.1}In_{0.9}Sb$ barrier layers are quantum wells or QWs, which were grown on GaAs substrates.

It is important to discuss transport properties of QWs of $InAs_xSb_{1-x}/(0 \leqq x \leqq 0.3)$ sandwiched between

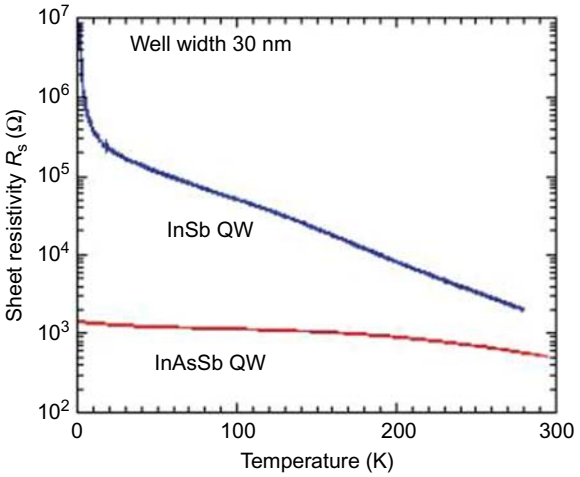

FIGURE 31.31 Temperature dependence of sheet resistivity of InSb and $InAs_{0.1}Sb_{0.9}$ QWs with a well width of 30 nm.

$Al_{0.1}In_{0.9}Sb$ barrier layers, as shown in Fig. 31.29A and B. The quantum wells may be written simply as $InAs_xSb_{1-x}/Al_{0.1}In_{0.9}Sb$ $(0 \leqq x \leqq 0.3)$, where $x = 0$ means InSb.

At first, low temperature properties of InSb and $InAs_{0.1}Sb_{0.9}$/ $Al_{0.1}In_{0.9}Sb$ quantum wells were measured.

In Fig. 31.31, temperature dependence of sheet resistivity of InSb and $InAs_{0.1}Sb_{0.9}$ QWs with a 30-nm-thick active layer are shown. The resistivity of InSb QWs increases remarkably with lowering the temperature, while that of $InAs_{0.1}Sb_{0.9}$ QWs shows a small increase below RT but does not rise very much even at a low temperature. Additionally, the resistivity of $InAs_{0.1}Sb_{0.9}$ QWs is much smaller than that of InSb QWs for the whole temperature range. Thus, sheet resistivity of the two types of QWs are quite different in spite of the little difference in addition of As only by $x = 0.1$.

The energy band diagrams of the quantum wells of $InAs_xSb_{1-x}/Al_{0.1}In_{0.9}Sb$ $(0 \leqq x \leqq 0.3)$ were recently calculated with respect to As content x; $x = 0$ (InSb QW), 0.1 ($InAs_{0.1}Sb_{0.9}$ QW), and 0.3 by using Poisson-Shroedinger solver. The band diagrams were useful to explain a difference in low temperature properties of the quantum wells (Manago et al., 2014, 2015a,b; Shibasaki et al., 2015).

Thus, to explain the sheet resistivity difference, we can use the energy band diagrams, which are shown in Fig. 31.32. The barrier layer was $Al_{0.1}In_{0.9}Sb$; the L_W of the active layer was 30 nm, and the temperature was 4 K. The calculated band diagrams of the $InAs_xSb_{1-x}/Al_{0.1}In_{0.9}Sb$ QWs show a transition from type I for InSb QW to type III via type II with increasing x. InSb QW ($x = 0$) shows a type I QW structure, and the bottom of the conduction band of InSb QWs is above the Fermi level (E_F). Therefore, no intrinsic electrons is not exited at low temperature, the well will be

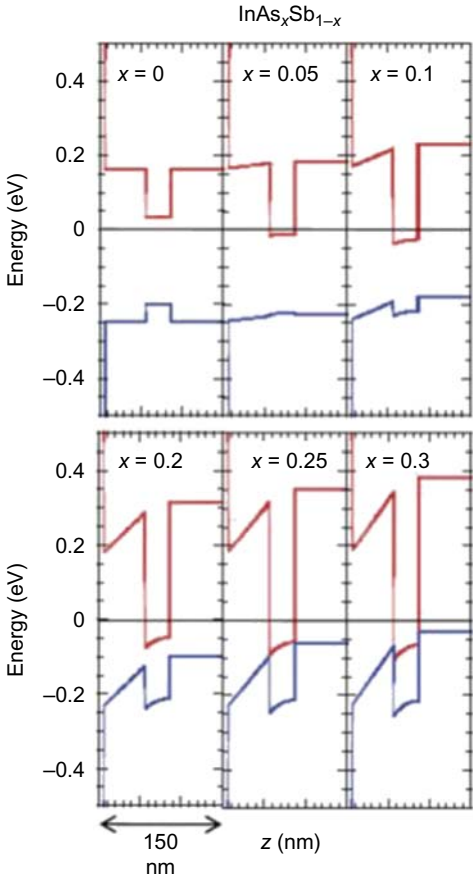

FIGURE 31.32 Energy band diagrams for InSb and InAsSb QWs of well width 30 nm with respect to As content x; $x = 0$ (InSb QW), 0.1 ($InAs_{0.1}Sb_{0.9}$ QW), and 0.3 ($InAs_{0.3}Sb_{0.7}$ QW).

depleted. For Type II QW of $InAs_{0.1}Sb_{0.9}$, the conduction band of the well moves under E_F. Thus, the $InAs_{0.1}Sb_{0.9}$ QWs are not depleted even at the low temperature. This result suggests that the carriers of the InAsSb QWs still remain in the conduction band at a low temperature and the sheet resistivity may be low at 4.2 K, corresponding to the experimental result shown in Fig. 31.31. At $x = 0$, the QW changes into the type III structure. In this band diagram transition, the bottom of the conduction band of the quantum well becomes lower with increasing x, and as a result, it lies under E_F. These results clearly explain the difference of the resistivity by carrier density difference at a low temperature between InSb and InAsSb QWs. Therefore, we concluded that the carrier density difference comes from the difference in the band diagram between the two kinds of QWs. This result is also verified by the measurement of carrier density at a low temperature of the QWs. The calculation showed a very small change of the energy band diagrams for various QW widths and temperatures, and the explanation of this section may not be changed, which was discussed in the cited references.

31.8 MAGNETORESISTANCE EFFECT OF INSB THIN FILMS GROWN ON GAAS SUBSTRATES BY MBE

MR effect is the change of resistance denoted by $\delta R/R_o$, which is proportional to the product of electron mobility and magnetic flux density, i.e.,

$$\frac{\delta R}{R_o} \propto (\mu B)^2.$$

A MR element with short bar electrodes is shown in Fig. 31.33. The single-crystal InSb thin films grown on GaAs substrates by MBE have a high electron mobility and show a very large MR effect. Experimentally, an example of a MR effect of InSb single-crystal thin films is shown in Fig. 31.34, where characteristics of InSb thin film were 1.0 μm thickness, electron mobility of 38,000 $cm^2\,V^{-1}\,s^{-1}$, and electron density of $7\times10^{16}\ cm^{-3}$. The MR device parameters used for fabricating practical MR shown in Fig. 31.33 were $W = 125\ \mu m$, $L = 24\ \mu m$, $L/W = 0.192$, length of short bar electrode size (metal width of short bar electrodes) 11 μm, and the separation of 1.249 mm between terminal electrodes.

The large MR effect of Sn-doped InSb single-crystal thin film is now used practically. The MR effect is small at small magnetic flux densities. The MR effect is proportional to the magnetic field change at larger magnetic flux densities, as shown in Fig. 31.34. Therefore, by the application of a suitable bias magnetic field by small permanent magnet to MR elements, the small change of magnetic flux density can be detected, where the resistance change is proportional to the detected magnetic field. MR elements are usually combined to form a bridge circuit for making an MR device. The MR devices combined with a small-size bias permanent magnet are used as a magnetic sensor of rotation sensors, which can detect the rotation of the spindle by using the iron gear attached to the spindle axis as shown in Fig. 31.35A. A photograph of such rotation sensors is shown in Fig. 31.35B. These rotation sensors are made with Sn-doped InSb single-crystal thin-film MR elements grown by MBE (Nishimura et al., 2003).

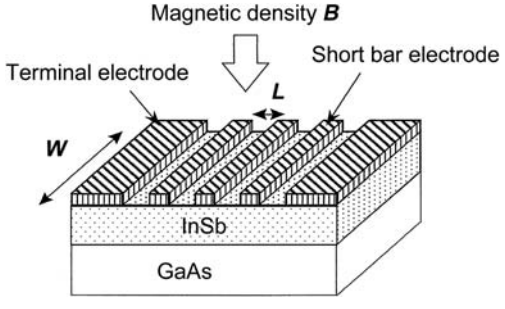

FIGURE 31.33 A MR element with short bar electrodes.

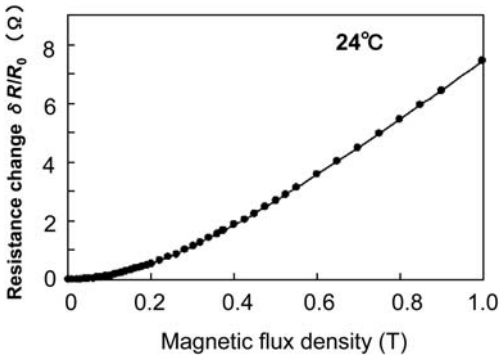

FIGURE 31.34 MR effect of Sn-doped InSb single-crystal thin film grown on GaAs substrate by MBE, $L/W = 0.192$, thickness = 1.0 μm, electron mobility = 38,000 $cm^2\,V^{-1}\,s^{-1}$, electron density = $7\times10^{16}\ cm^{-3}$.

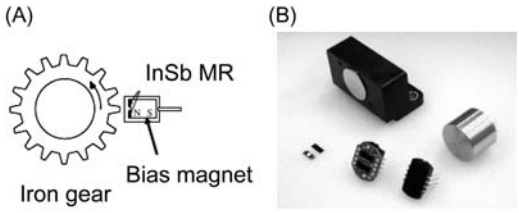

FIGURE 31.35 InSb MR rotation sensors (A) principle of MR rotation sensor; (B) photograph of InSb MR rotation sensors.

31.9 UNCOOLED INSB PHOTOVOLTAIC INFRARED SENSORS

31.9.1 Introduction of Infrared Sensor Technology

Pyroelectric sensors are generally used to detect weak infrared irradiation due to their high sensitivities at room temperature. However, they require the use of metallic packages to insulate the sensitive element from thermal disturbances and electromagnetic noise, making their miniaturization difficult. Moreover, it is difficult for the pyroelectric sensors to detect a stationary human body because the surface charge generated on the pyroelectric element disappears gradually when the human body is stationed. Thermopile infrared sensors, which are used in remote thermometry, are also available, but they require the same thermal isolation technique and are unable to respond to fast signals. As the sensitivity of thermopiles is one order of magnitude lower than pyroelectric infrared sensors, the

application of thermopiles is thus limited to proximity sensing.

HgCdTe (MCT) is a well-established system, which has been the dominant system for mid- and long-wavelength infrared photon detectors. Serially connected MCT photovoltaic detectors on CdZnTe substrates have also been developed to increase the output voltage (Piotrowski and Gawron, 1995; Piotrowski and Razeghi, 1995). However, MCT suffers from instability problems due to the high vapor pressure of Hg, and the CdZnTe substrate is not readily available in large sizes.

Meanwhile, InAsSb photodiode detectors operating near room temperature have also been reported (Kim et al., 1995; Razeghi, 1998). However, their responsivity is known to be limited by Auger recombination, making the photogenerated signal from the detectors insufficient to drive conventional amplifiers. Consequently, an AlInSb barrier layer was proposed to suppress the Auger processes by decreasing the free carrier concentration to below its equilibrium value (Ashley et al., 1991). However, Auger-suppressed nonequilibrium photodiodes suffer from $1/f$ noise; hence, high sensitivity can be obtained only at high frequencies (Elliott et al., 1997). For the same reason, conventional infrared detectors using InSb require cooling systems (Chen, 2002).

On the other hand, the InSb photovoltaic infrared sensors that we developed can operate at room temperature in a photovoltaic mode, and no thermal insulation is required, enabling their miniaturized plastic molding (Kuze et al., 2006, 2007, 2009; Camargo et al., 2007). We describe herein InSb thin films grown on GaAs substrate by MBE that have potential for use in the fabrication of low-cost millimeter-sized infrared sensors with considerable sensitivity at room temperature. Their potential applications include noncontact thermometry as well as human body irradiation detection.

31.9.2 InSb Photovoltaic Infrared Sensors Grown by MBE

31.9.2.1 Growth and Device Fabrication of InSb Photovoltaic Infrared Sensor

The schematic structure and a band diagram of an InSb photovoltaic sensor thin film structure are shown in Fig. 31.36. The InSb photovoltaic sensor structure was grown on a semiinsulating GaAs (100) substrate by a Riber MBE-49 system, equipped with elemental group III solid sources and valved cracker cells for arsenic and antimony. The film consists of an epitaxial growth of a 1-μm-thick n^+-InSb layer, followed by a 2-μm-thick p^--InSb absorber layer. To reduce the diffusion of photoexcited electrons, a 20-nm-thick p^+-$Al_{0.17}In_{0.83}Sb$ barrier layer was grown on the p^--InSb layer. Finally, a 0.5-μm-thick p^+-InSb layer was grown as the top contact. The n-type and p-type dopants were Sn and Zn, respectively, with concentrations of $7\times10^{18}\,cm^{-3}$ for the n^+ layer, $6\times10^{16}\,cm^{-3}$ for the p^- layer, and $2\times10^{18}\,cm^{-3}$ for the p^+ layer. The doping concentrations were determined by secondary ion mass spectroscopy.

The large lattice mismatch of more than 14.6% between InSb and GaAs substrate generates high concentrations of misfit dislocations at the interface of InSb/GaAs. However, the strain relaxation of InSb was very fast and the reflection high-energy electron diffraction pattern turned into a strongly streaked pattern after growing only a 50-nm-thick InSb layer with no buffer layers on the GaAs substrate. The misfit dislocation density of InSb layers was around $6-8\times10^8/cm^2$ by cross-sectional high-resolution transmission electron microscopy (X-TEM) analysis. Moreover, the etch pit density of the surface of the InSb photovoltaic infrared sensor structure was observed to be about $1\times10^9/cm^2$ after etching by 0.2 μm of p^+-InSb top contact layer using $HF/HNO_3/H_2O$ etchant.

The $p^+ - p^- - n^+$ photodiodes were electrically isolated by etching a mesa structure first to an intermediate depth in the n^+-InSb layer before a subsequent etching all the way to the substrate. Afterwards, a 300-nm-thick Si_3N_4 passivation layer was grown using plasma chemical vapor deposition (CVD), while Ti/Au ohmic contacts were formed by evaporation and a lift-off process. Finally, a 300-nm-thick SiO_2 passivation layer, also grown by plasma CVD, was deposited over the metallic layer.

In order to verify the metal/InSb interface behaviors as well as their contact resistances at room temperature, Au/Ti/p^+-InSb/Ti/Au and Au/Ti/n^+-InSb/Ti/Au planar resistors were fabricated. From the I–V measurements of p^+ and n^+ resistors at room temperature, we confirmed ohmic characteristics between bias voltage of −0.3 and 0.3 V (Camargo et al., 2006). We obtained metal/p^+-InSb layer and metal/n^+-InSb layer contact resistances on the order of 10^{-6} and $10^{-7}\,\Omega\,cm^2$, respectively, which could be negligible in the photodiodes.

To improve the S/N ratio of the InSb photovoltaic sensor, 910 photodiodes were patterned on a $700\times700\,\mu m^2$ chip and were connected in series, as shown in Fig. 31.37. The length of a single InSb photovoltaic sensor was 20 μm. The absorber region of a single InSb photovoltaic sensor was almost octagonal in shape, and its area was about $100\,\mu m^2$. Output voltage was almost independent on the single photodiode junction area, being proportional to the number of connected photodiodes n. Leakage current between

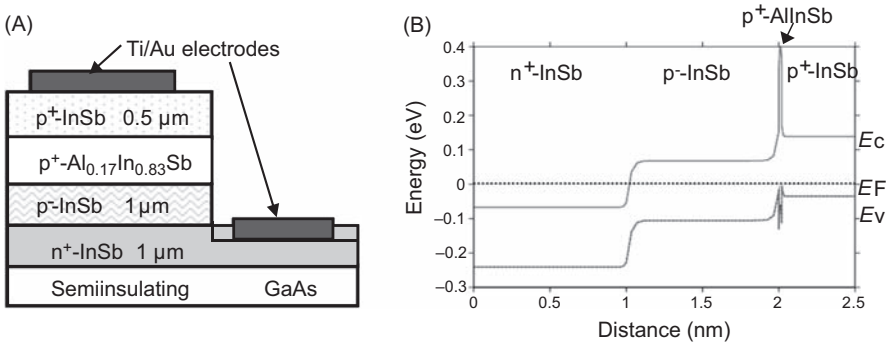

FIGURE 31.36 (A) Schematic structure and (B) energy band diagram of InSb photovoltaic infrared sensor.

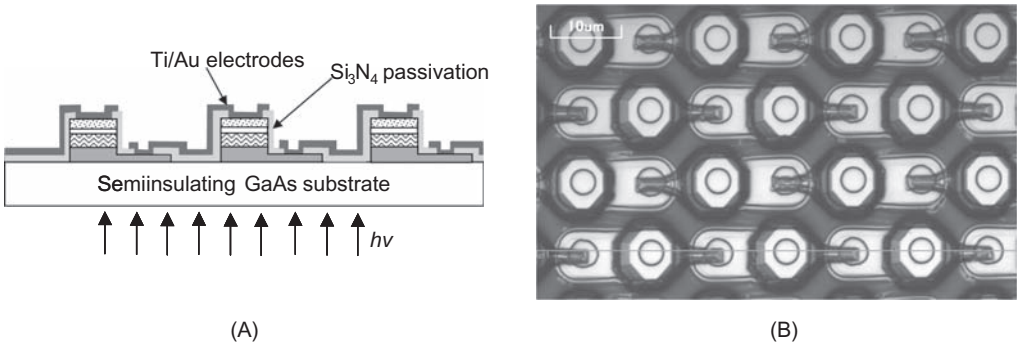

FIGURE 31.37 (A) Schematic structure of InSb infrared sensor made of multiple photodiodes connected in series and (B) photograph of top view of InSb infrared sensor chip taken using a laser microscope.

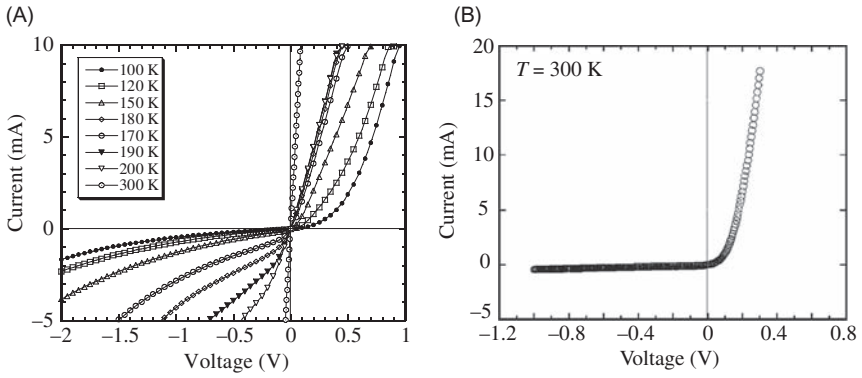

FIGURE 31.38 Current–voltage characteristics of (A) a single $p^+ - p^- - n^+$ InSb infrared sensor without AlInSb barrier layer and (B) InSb photovoltaic infrared sensor with AlInSb barrier layer with junction area of 81 μm^2.

photodiodes was negligible, which could be concluded from the proportional relation between the nonbias differential resistance R_0 and n (Camargo et al., 2006). Due to the nonbias operation, noise was equivalent to the thermal noise due to R_0. Since R_0 is proportional to n, noise increases with a factor of $n^{1/2}$. As a result, as n increases, SNR is improved by a factor of $n^{1/2}$.

31.9.2.2 *Effect of the AlInSb Barrier Layer*

The current–voltage curves of a single InSb photovoltaic sensor with and without an AlInSb barrier layer are shown in Fig. 31.38. In the $p^+ - p^- - n^+$ photodiode, the $I-V$ curve was almost linear at room temperature. This indicates that the top and the bottom contacts of the p^+-InSb/p^--InSb/n^+-InSb mesa

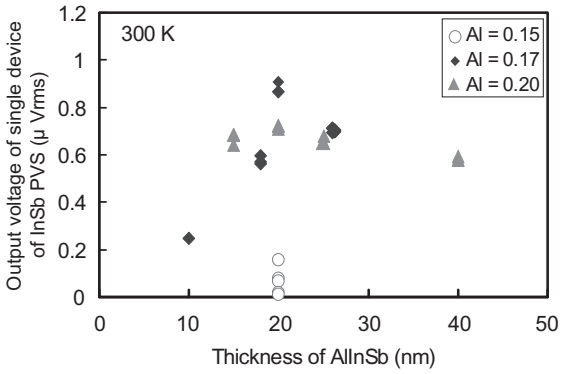

FIGURE 31.39 Output voltage of InSb photovoltaic infrared sensor (PVS) as a function of a thickness of $Al_xIn_{1-x}Sb$ barrier layer ($x = 0.15-0.2$).

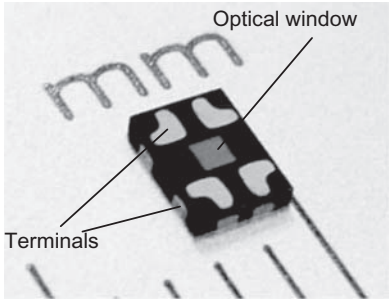

FIGURE 31.40 Photograph of a DFN packaged InSb photovoltaic infrared sensor.

structure were ohmic at room temperature. As the temperature was reduced from 300 to 100 K, the dark current was gradually decreased. The rectifying characteristic is clearly visible for temperatures less than 150 K. On the other hand, owing to the introduction of the AlInSb barrier layer between p^+-InSb and p^--InSb, the diffusion of photoexcited electrons to the p^+-InSb layer was suppressed, and the dark current of the InSb photovoltaic sensor was markedly decreased. As a result, a very good rectifying characteristic was obtained at room temperature, as shown in Fig. 31.38B.

To investigate the effect of the AlInSb barrier layer, we studied the output voltage dependence on the Al composition x and the thickness of $Al_xIn_{1-x}Sb$. The Al composition x and the thickness of AlInSb were changed from 0.15 to 0.20 and from 10 to 40 nm, respectively. Fig. 31.39 shows the output voltage dependence on the Al composition and the thickness of the $Al_xIn_{1-x}Sb$ barrier layer. With an Al composition of 0.15, the barrier effect of AlInSb was not enough to suppress the diffusion of photoexcited electrons. The thickness of the AlInSb barrier layer needed to be at least more than 15 nm. As we increased the thickness of the barrier layer, the output voltage of the InSb photovoltaic infrared sensor decreased gradually. The optimum condition of the Al composition and the thickness of $A_xIIn_{1-x}Sb$ barrier layer showed to be $x = 0.17$ and 20 nm, respectively.

31.9.3 Device Performance of InSb Photovoltaic Infrared Sensors

31.9.3.1 Miniaturized Packaging

Packaging was a key element in the system miniaturization. Contrary to pyroelectric or other thermal sensors, the InSb photovoltaic infrared sensor does not require the sensing element suspension or gas-filled packages. This allowed the use of a standard dual flat nonleaded (DFN) packaging method to encapsulate the InSb photovoltaic infrared sensor. In addition, a unique technique was used to open a window on the detector side, which exposed the backside of the GaAs substrate allowing infrared light incident, as shown in Fig. 31.40. This InSb photovoltaic infrared sensor was commercialized as a product (Product number; IR1011) by Asahi Kasei Microdevices Corporation. The InSb infrared sensor can also be packaged together with a Si-CMOS integrated circuit (IC) for signal preamplification. Amplified sensors can also be implemented, and in this case the Si-CMOS IC is replaced by a Si interposer.

The mounting process consists of flip-chip bonding of the GaAs detector chip on the Si-interposer, connection with external pads, molding, and window opening. In the case of the amplified sensor, with the flip-chip bonding process, short electric connections are achieved between the InSb sensor and the preamplifier, making the system immune to electromagnetic interferences.

Using the sensor substrate as a window, the number of components was reduced and the packaging process could be simplified. The final external dimensions were $1.9\,\text{mm} \times 2.7\,\text{mm} \times 0.4\,\text{mm}$, which allowed a wide range of applications as in noncontact thermometers or human body irradiation detection in mobile equipment.

31.9.3.2 Responsivity of InSb Photovoltaic Infrared Sensors

A 500 K cavity blackbody equipped with a wheel chopper was used as a light source for chopped responsivity measurements, which were performed at room temperature. Fig. 31.41 shows the 700-element InSb photovoltaic infrared sensor response and noise compared with those of a commercially available pyroelectric sensor. The responsivity R_v of the InSb photovoltaic infrared sensors, calculated using 700 times the

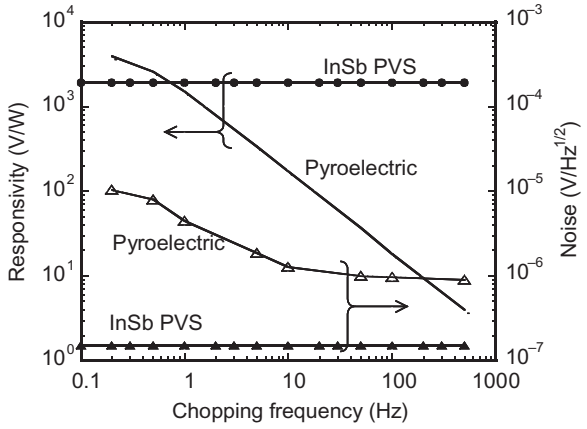

FIGURE 31.41 Comparison of responsivity and output noise at 300 K between the InSb photovoltaic infrared sensor (InSb PVS) and a conventional pyroelectric sensor.

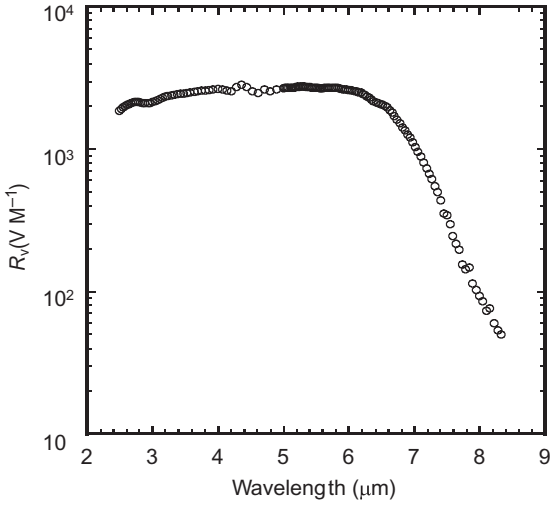

FIGURE 31.42 Spectral response of InSb photovoltaic infrared sensor at 300 K.

absorber area of a single photodiode, was almost the same as that of the pyroelectric sensor around the frequency of 1 Hz, being kept constant for signals ranging from DC to 500 Hz.

In the case of the pyroelectric sensor, the voltage generated in the pyroelectric element disappears when no thermal variation occurs. For this reason, it is not able to detect a constant irradiation signal. Moreover, since its output depends on the temperature variation of the pyroelectric element after infrared absorption, its responsivity is lowered at high chopping frequencies.

Noise of the 700-element InSb photovoltaic infrared sensors was measured using an external preamplifier coupled to a dynamic signal analyzer. To reject electromagnetic noises, the sensor and the external amplifier were introduced into a shield box.

The packaged InSb photovoltaic infrared sensor was immune to thermal fluctuations and $1/f$ noise, being equivalent to its thermal noise, which is much lower than the pyroelectric sensor. As a result, R_v of 1.9 kV W^{-1} and detectivity (D^*) of 2.8×10^8 cm $Hz^{1/2}$ W^{-1} were obtained.

When operated at photovoltaic mode, the InSb infrared sensor outputs showed satisfactory signal levels at room temperature, with no cooling systems or thermal insulation, allowing their miniaturized packing. In addition, there is no power consumption, since the photoelectric signal is generated without bias current, which makes the device suitable for applications in low-power mobile devices. The InSb photovoltaic sensor also works as an absolute irradiation detector, being able to detect even the presence of the static human body.

31.9.3.3 Spectral Response

Spectral response was measured using a monochromator equipped with ceramic heater light source and chopper. An IPHT TS-100 calibrated thermopile, which has a flat response in a wide wavelength range, was used as a reference. The output of InSb photovoltaic infrared sensor as well as the reference thermopile was measured at a chopping frequency of 1 Hz at which the thermopile has a higher response, with 35670 A dynamic signal analyzer, allowing us to obtain the absolute responsivity in function of wavelength. Fig. 31.42 shows the measurement result for a 700-element InSb sensor, which showed peak responsivity between 5 and 6 μm and cutoff wavelength of 6.8 μm. At lower wavelengths, the responsivity is supposed to be limited by the GaAs substrate transmittance, with cutoff wavelength around 1 μm. With this spectral response, the InSb photovoltaic infrared sensor is able to detect the mid-IR irradiation from the human body.

31.9.4 Temperature Measurement Application of InSb Photovoltaic Infrared Sensors

31.9.4.1 Irradiance Dependence of the Photocurrent

The irradiance dependence of the photocurrent of InSb photovoltaic infrared sensor was evaluated at room temperature. The InSb photovoltaic infrared sensor was back-illuminated with a CI Systems SR-20 cavity blackbody set at a temperature of 500 K and a chopping frequency of 10 Hz. A Si wafer was used as an optical filter, and the distance between the sample and the blackbody aperture was 10 cm. Irradiance of the light emitter was varied by adjusting the aperture area and measured by a calibrated Eppley thermopile. The irradiance dependence of the photocurrent of the

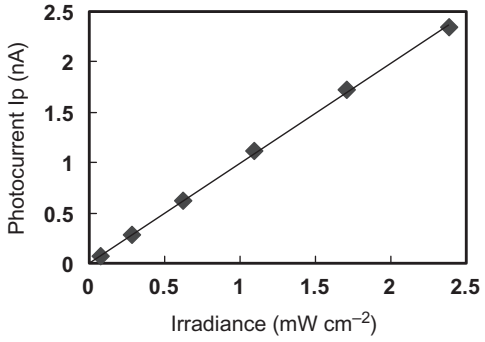

FIGURE 31.43 The photocurrent of InSb photovoltaic infrared sensor at 298 K as a function of irradiance, using a cavity blackbody at 500 K.

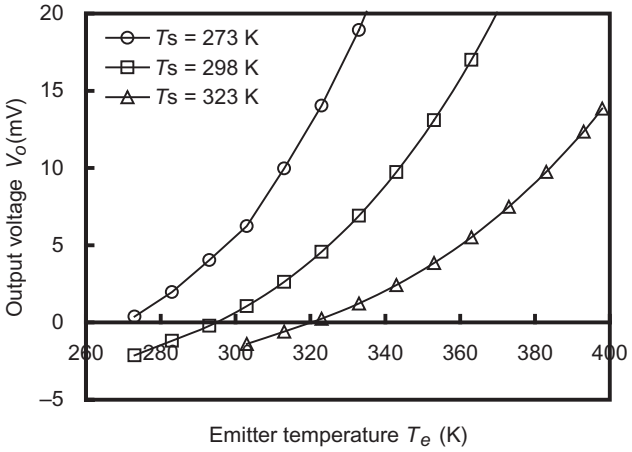

FIGURE 31.44 The output voltage of InSb photovoltaic infrared sensor at different sensor temperatures (T_s) as a function of the emitter temperature (T_e).

InSb photovoltaic infrared sensor is shown in Fig. 31.43. Photocurrent I_p is defined as

$$I_p = \frac{V_o}{R_o}, \tag{31.1}$$

where V_o and R_o are the output voltage and resistance of InSb photovoltaic infrared sensor, respectively. R_o is defined as

$$R_o = \left(\frac{\partial I}{\partial V}\right)^{-1}_{v=0} \tag{31.2}$$

where I and V are the bias current and voltage, respectively. As shown in Fig. 31.43, the photocurrent of the InSb photovoltaic infrared sensor was directly proportional to the aperture area, indicating its linear dependence on the irradiance.

31.9.4.2 Temperature Dependence of Sensitivity and Responsivity

The temperature dependence of sensitivity was measured using a CI system SR-800 flat blackbody with an emitter area of $10 \times 10\,\text{cm}^2$. The distance between the sensor and the blackbody was 10 cm, and the system was inserted into an oven to allow the sensor temperature to equilibrate.

The output voltage of InSb photovoltaic infrared sensor at different sensor temperatures T_S as a function of emitter temperature T_E was evaluated. As shown in Fig. 31.44, the output voltage varied as a function of the sensor temperature. As the sensor temperature decreased, the output voltage of InSb photovoltaic infrared sensor increased due to the decrease in the number of intrinsic carriers in InSb and the suppression of Auger recombination. When the emitter temperature T_E was lower than the sensor temperature T_S, the output voltage was negative since the output voltage is proportional to the energy difference E between the emitter and InSb photovoltaic infrared sensor.

The spectral irradiance $K(\lambda, T)$ emitted from a body with temperature T is represented as

$$K(\lambda, T) = \frac{2\pi hc^2}{\lambda^5}\frac{1}{e^{ch/\lambda kT} - 1}, \tag{31.3}$$

where λ is the wavelength; c is the light speed, and h and k are Planck and Boltzmann constants, respectively.

For a given wavelength λ, the energy difference $E(\lambda)$ becomes

$$E = K(\lambda, T_E) - K(\lambda, T_S). \tag{31.4}$$

Furthermore, the output voltage is proportional to the light absorbance $A(\lambda)$ of the active layer. The light absorbance $A(\lambda)$ is calculated using Fresnel's law with refractive index n, k and thickness for each of the films of the InSb photovoltaic infrared sensor. Finally, the output voltage V_o becomes

$$\begin{aligned} V_o &= \alpha \int E(\lambda) \times A(\lambda) \mathrm{d}\lambda \\ &= \alpha \int (K(\lambda, T_E) - K(\lambda, T_S)) \times A(\lambda) \mathrm{d}\lambda, \end{aligned} \tag{31.5}$$

where α is a constant factor, depending on the experimental conditions such as an emitter size and distance from the sensor to the emitter.

We estimated the output voltage using Eq. (31.5), where the experimental output voltage at a sensor temperature of 298 K was compared with a theoretical fit, as shown in Fig. 31.45. The output voltage was normalized by the data obtained at an emitter temperature of 393 K. Fig. 31.45 shows that the experimental output voltage coincided with the theoretical calculations; similar agreements were also found at sensor temperatures of 273 and 323 K.

The result indicates that the InSb photovoltaic infrared sensor can precisely measure the absolute

temperature of an emitting object once the temperature of the InSb photovoltaic infrared sensor itself is known.

The sensitivity $\Delta V/\Delta T$ of the InSb photovoltaic infrared sensor at room temperature was estimated from Fig. 31.44 to be 127 μV K^{-1}. Since the InSb photovoltaic infrared sensor operated in photovoltaic mode, the noise of the InSb photovoltaic infrared sensor consisted only of white noise of 0.13 μV_{RMS} Hz$^{-1/2}$. A noise equivalent temperature difference of 1.0 mK Hz$^{-1/2}$ was calculated using both the sensitivity and the noise data. These results demonstrate the capability of the InSb photovoltaic infrared sensor for applications in precise noncontact thermometry. Furthermore, since the detector operates at room temperature and has millimeter dimensions, it is also well suited for applications in portable devices.

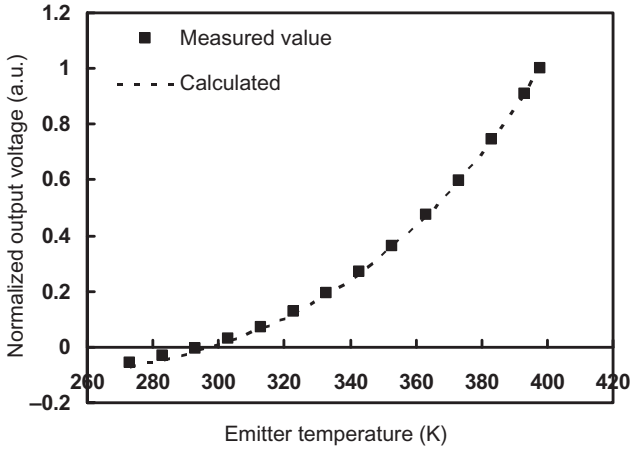

FIGURE 31.45 The output voltage of InSb photovoltaic infrared sensor at a sensor temperature of 298 K, normalized by the output voltage at an emitter temperature of 393 K, showing both the experimental data (bold) and the theoretical fit (dashed).

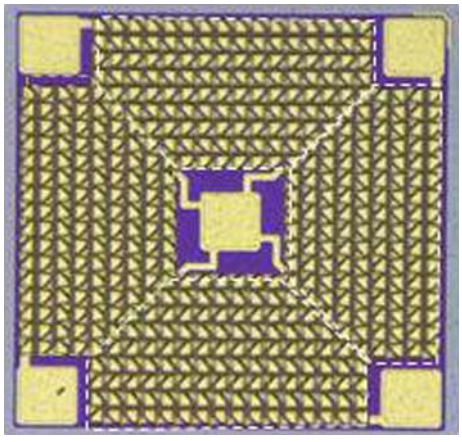

FIGURE 31.46 Photograph of top view of 4 pixcels InSb IR sensor chip taken using a laser microscope.

31.9.5 Human Body Detection of Infrared Sensor With Signal Processing IC

In order to achieve human body detection using our InSb photovoltaic infrared sensor, the four pixcels InSb IR sensors in one-chip were developed. Fig. 31.46 shows the plain view photograph of four pixcel IR sensors from the top. We have also developed the algorithm for detecting the moving direction of human body. Moreover, an integrated circuit was designed and fabricated to compensate the temperature dependence and amplifier with digital output, as shown in the block diagram of Fig. 31.47. It has been commercialized as a product (Product number; AK9750) by Asahi Kasei Microdevices Corporation (Fig. 31.48). In order to avoid mis-detection by the noise-like sunlight, the optical filter to cut the light of shorter wavelength than 5 μm was placed in front of the IR sensor chip.

AK9750 is a sensor IC, which integrates four channel (4ch) infrared sensors, a signal processing IC, a field of view limiter for determining detection area, and an optical filter. Human body detection can be easily achieved by this integration. AK9750 provides 16-bit digital output in I2C format after calibrating an offset and gain variation of each sensor element by the signal processing IC. This device can detect human presence not only in motion but also not in motion because it converts infrared of the human body to electrical signal directly. AK9750 has already been adopted for a human body detection sensor in personal

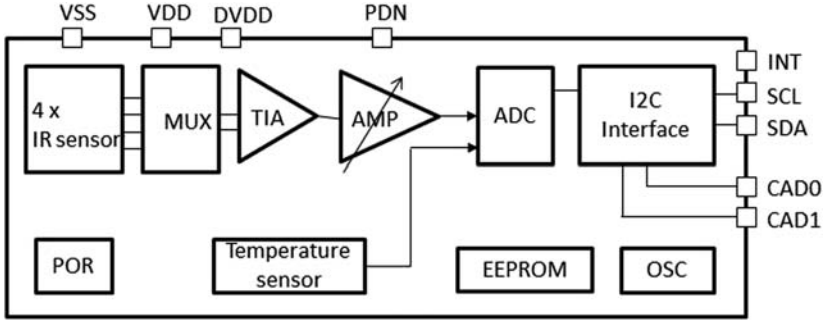

FIGURE 31.47 Block diagram of 4 pixcels InSb IR sensor with signal processing IC.

computers, internet of things applications, and household equipment.

31.9.6 Nondispersive Infrared Gas Sensor Using the InSb IR Sensor

The wavelength sensitivity of the InSb infrared sensors is in the range of 7 μm from 3 μm, as shown in Fig. 31.42. Many important gases, such as CO_2, CO, and NO, have a strong characteristic absorption in the mid-infrared region. The InSb infrared sensor is suitable for sensing these gases. We applied the InSb IR sensors to the nondispersive infrared (NDIR) sensor to monitor CO_2 gas concentration in real time. The fundamental module structure and photograph of the NDIR sensor using the InSb IR sensors is shown in Fig. 31.49. Two InSb IR sensors were used for measuring the concentration of CO_2; the first sensor (S1) is for CO_2 gas sensing, and the second one (S2) is for reference. The optical filters were placed in front of the InSb sensors; one is a 4.3 μm band-pass filter for CO_2 gas sensing; the other one is a 3.9 μm band-pass filter for reference (no absorption). The length of the gas cell was 20 and 40 mm. The CO_2 gas concentration was measured by calculating the rate S1/S2 of the signals from S1 and S2. The gas sensing responsivity of the InSb NDIR sensor was shown in Fig. 31.50. Because it has very quick responsivity, it enables the low-power consumption of the gas sensing module. We were able to confirm the good linearity of the logarithmic rate S1/S2 as a function of CO_2 concentration as shown in Fig. 31.51. The CO_2 concentration

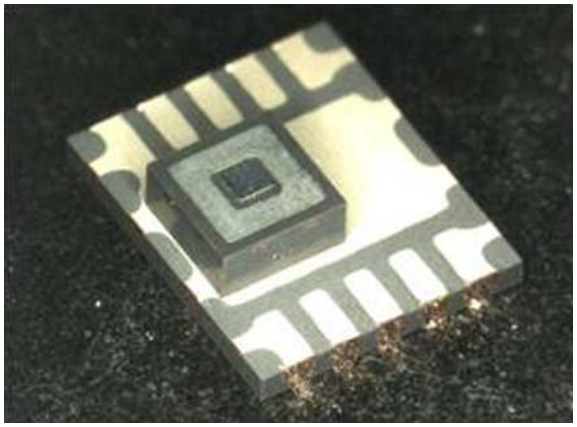

FIGURE 31.48 Photograph of an IR sensor IC (AK9750).

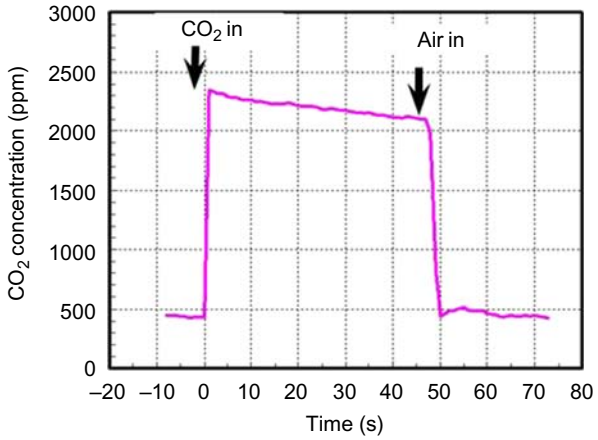

FIGURE 31.50 Responsivity characteristics of the InSb NDIR gas sensor.

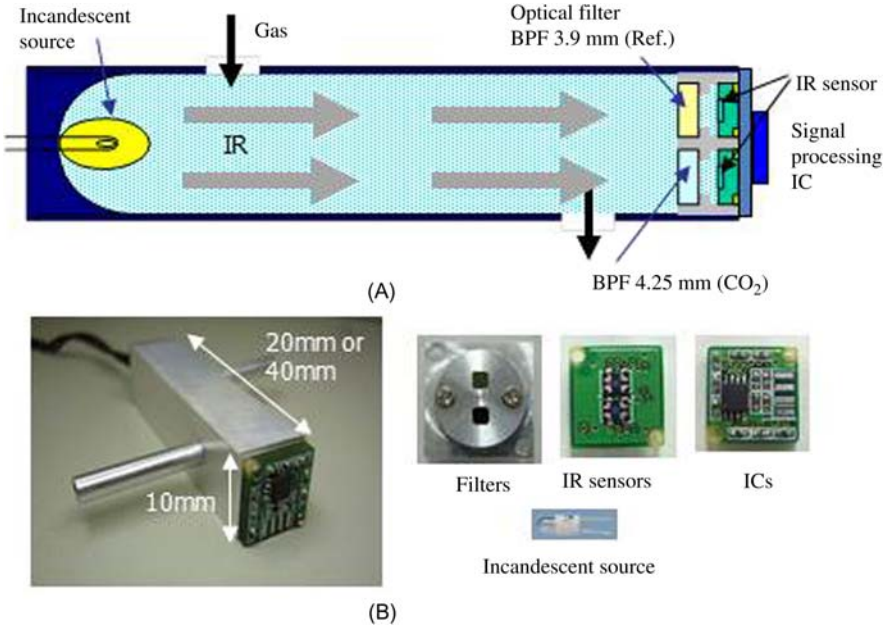

FIGURE 31.49 (A) Schematic structure of NDIR gas sensor using IR sensors and (B) photographs of the NDIR gas sensor module we demonstrated.

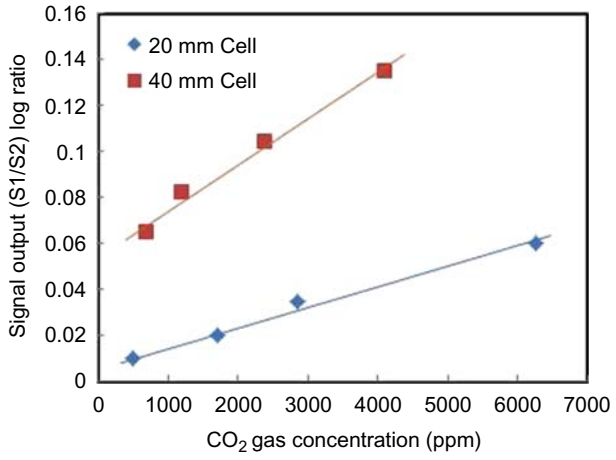

FIGURE 31.51 Output signal of InSb NDIR gas sensor module at 20 and 40 mm cell length, as a function of CO_2 gas concentration.

can be obtained in real time by using this calibration data. If you use the InSb NDIR sensor, which we developed, and monitor the CO_2 concentration in the office, home, and car cabin, it can always maintain a good air quality and can save energy by taking fresh air only when it is necessary.

31.10 SUMMARY

In this chapter, we have discussed mass production of magnetic sensors and infrared sensors using narrow-bandgap compound semiconductor materials such as InSb, InAs, and related antimonides grown by MBE. We showed that the MBE system is suitable for the mass production of these sensors. Now Hall sensors produced by MBE are widely used for various electric apparatuses, mobile phones, digital cameras, and automobile applications. Moreover, a miniaturized InSb photovoltaic infrared sensor operating at room temperature was demonstrated. The InSb photovoltaic infrared sensor was encapsulated in a very small package. The photocurrent of the infrared sensor showed good linear dependence on irradiance power. The output voltage of the InSb photovoltaic infrared sensor was proportional to the light absorbance of the active layer of the sensor and the energy difference between the emitter and the sensor. The InSb photovoltaic infrared sensor, with its high sensitivity, ease of manufacture, and millimeter dimensions, is a promising device for both noncontact thermometry and human body detection in portable device applications. The 4ch InSb infrared sensors with IC were demonstrated for human body detection. The InSb IR sensor was also applied to the NDIR gas sensor module to monitor CO_2 gas concentration in real time.

References

Ashley, T., Dean, A.B., Elliott, C.T., McConville, C.F., Pryce, G.J., Whitehouse, C.R., 1991. Ambient temperature diodes and field-effect transistors in InSb/$In_{1-x}Al_xSb$. Appl. Phys. Lett. 59, 1761.

Camargo, E.G., Kuze, N., Ueno, K., Kawakami, Y., Moriyasu, Y., Nagase, K., et al., 2006. Miniaturized InSb photovoltaic infrared sensor operating at room temperature. Proc. SPIE 6189, 618902–1.

Camargo, E.G., Ueno, K., Morishita, T., Sato, M., Endo, H., Kurihara, M., et al., 2007. High-sensitivity temperature measurement with miniaturized InSb mid-IR sensor. IEEE Sensors J. 7, 1335.

Chen, L.P., 2002. Advanced FPAs for multiple applications. Proc. SPIE 4721, 1.

Cho, A.Y., Arthur, J.R., 1972. Molecular beam epitaxy. Prog. Solid State Chem. 10, 157.

Elliott, C.T., Gordon, N.T., Hall, R.S., Phillips, T.J., Jones, C.L., Best, A., 1997. 1/f noise studies in uncooled narrow gap $Hg_{1-x}Cd_xTe$ non-equilibrium diodes. J. Electron Mater. 26 (6), 643.

Geka, H., Okamoto, Yamada, S., Goto, H., Yoshida, K., Shibasaki, I., 2007. Properties of InSb single crystal thin films sandwiched by $Al_{0.1}In_{0.9}Sb$ layers with 0.5% lattice mismatch grown on GaAs. J. Cryst. Growth 301/302, 152.

Guenther, K.G., 1958a. Aufdampfschichten aus halbleitenden III–V Verbindungen. Z. Naturforschung 13a, 1081.

Guenther, K.G., 1958b. Aufdampfschichten aus halbleitenden III–V Verbindungen. Naturwissenschaften 45, 415.

Iwabuchi, T., Ito, T., Ymamoto, M., Sako, K., Kanayama, Y., Nagase, K., et al., 1995. High sensitivity Hall elements made from Si doped InAs on GaAs substrates by molecular beam epitaxy. J. Cryst Growth 150, 1307.

Kataoka, S., 1965. Magneto-Electric Transducers. Nikkan Kogyo Shimbun Press, Tokyo.

Kim, J., Kim, S., Wu, D., Wojkowski, J., Xu, J., Piotrowski, J., et al., 1995. 8–13 μm InAsSb heterojunction photodiode operating at near room temperature. Appl. Phys. Lett. 67, 2645.

Kuze, N., Nagase, K., Muramatsu, S., Miya, S., Iwabuchi, T., Ichii, A., et al., 1995. InAs deep quantum well structures and their application to Hall elements. J. Cryst. Growth 150, 1307.

Kuze, N., Goto, H., Miya, S., Muramatsu, S., Matsui, M., Shibasaki, I., 1996. Molecular beam epitaxial growth of InAs/AlGaAsSb deep quantum wells on GaAs substrates. Mater. Res. Soc. Symp. Proc. 399, 168.

Kuze, N., Goto, H., Matsui, M., Shibasaki, I., Sakaki, H., 1997. Molecular beam epitaxial growth of high electron mobility InAs/AlGaAsSb deep quantum well structures. J. Cryst. Growth 175/176, 868.

Kuze, N., Camargo, E.G., Ueno, K., Kawakami, Y., Moriyasu, Y., Nagase, K., et al., 2006. Microchip-sized InSb photodiode infrared sensors operating at room temperature. Phys. Status Solid. (c) 3 (3), 431.

Kuze, N., Camargo, E.G., Ueno, K., Morishita, T., Sato, M., Kurihara, M., et al., 2007. High performance miniaturized InSb photovoltaic infrared sensors operating at room temperature. J. Cryst. Growth 301–302, 997.

Kuze, N., Morishita, T., Camargo, E.G., Ueno, K., Yokoyama, A., Sato, M., et al., 2009. Development of uncooled miniaturized InSb photovoltaic infrared sensors for temperature measurement. J. Cryst. Growth 311, 1889.

Manago, T., Ishida, S., Geka, H., Shibasaki, I., 2014. Recent developments in narrow gap semiconductor InSb and InAsSb quantum wells. J. Vacu. Soc. Jpn 57 (7), 201.

Manago, T., Ishida, S., Geka, H., Shibasaki, I., 2015a. Relationship between transport properties and band diagrams in $InAs_xSb_{1-x}/Al_{0.1}In_{0.9}Sb$ quantum wells. AIP Adv. 5, 067149. Available from: https://doi.org/10.1063/1.4923192.

Manago, T., Ishida, S., Geka, H., Shibasaki, I., 2015b. Interfacial trap states and improvement of low-temperature mobility by doping in InSb/AlInSb quantum wells. J. Appl. Phys 117, 065701. Available from: https://doi.org/10.1063/1.490780.

Nagase K., Muramatsu S., Kuze N., Ichii A., Shibasaki I., Mori K. 1993. InAs/AlGaAsSb quantum well Hall elements having high output voltage and good temperature characteristics. In: Digest of Technical Papers; Abstract of Late News Papers, The 7th International Conference on Solid-State Sensors and Actuators, p. 34.

Nishimura, K., Goto, H., Geka, H., Okamoto, A., Shibasaki, I., 2003. Properties and application of Sn-doped InSb single crystal thin film magnetoresistance elements. Proceedings of the 20th Sensor Symposium. IEEJ, Japan, p. 161.

Okamoto, A., Shibasaki, I., 2003. Transport properties of Sn doped InSb thin films and application to Hall elements. J. Cryst. Growth 251, 560.

Okamoto, A., Ashihara, A., Akaogi, T., Shibasaki, I., 2001. InSb thin films grown on GaAs substrate and their magneto-resistance effect. J. Cryst. Growth 227/228, 619.

Piotrowski, J., Gawron, W., 1995. Extension of long wavelength IR photovoltaic detector operation to near room temperature. Infrared Phys. Technol. 36, 1045.

Piotrowski, J., Razeghi, M., 1995. Improved performance of IR photodetectors with 3D gap engineering. Proc. SPIE 2397, 180.

Razeghi, M., 1998. Current status and future trends of infrared detectors. Opto-Electron. Rev. 6 (3), 155.

Sakai, Y., Ohshita, M., 1960. Preparation of indium antimonide films and measurement of hall characteristics. J. IEE Jpn 80, 166.

Shibasaki I. 1984. Properties of Hall Elements by Vacuum Deposition, the Correction of Advanced Technology of Semiconductor Devices (Multi-authors book, in Japanese).Keiei System Kennkyusyo, Shinjyuku, Tokyo [Chapter 3], Sec. 11, p. 373.

Shibasaki, I., 1988. High sensitivity InSb Hall elements and their development for practical use. Monthly Report Jpn Soc. Chem. Indus. 41 (5), 12.

Shibasaki I. 1989. High sensitive Hall element by vacuum deposition. In: IEE Japan, Technical Digest on 8th Sensors Symposium, p. 211.

Shibasaki I. 1995. The practical Hall elements as magnetic sensors by thin film technology. In: IEEE Lasers and Electro-Optics Society 1995 Annual Meeting, Conference Proceedings, vol. 1, p. 85.

Shibasaki, I., 1997. Mass production of InAs Hall elements by MBE. J. Cryst. Growth 175/176, 13.

Shibasaki, I., 2000. Magnetic sensors and magnetometers. In: Pavel, Ripka (Ed.), High Electron Mobility Thin Film Hall Elements. Artech House, Boston, MA/London, p. 184. , Chapter 5. 2.

Shibasaki I., Kanayama Y., Ito T., Ichimori F., Yoshida T., Nagase K., et al. 1991. High sensitive thin film InAs Hall element by MBE, IEEE. In: Digest Tech. Papers on Transducers, p. 1069.

Shibasaki, I., Geka, H., Okamoto, A., Shibata, Y., 2005. The thickness dependence of InAs sandwiched by AlGaAsSb layers grown by MBE. J. Cryst. Growth 278, 162.

Shibasaki, I., Geka, H., Okamoto, A., 2009. Transport properties of InSb and $InAs_{0.1}Sb_{0.9}$ thin films between $Al_{0.1}In_{0.9}Sb$ layers grown by molecular beam epitaxy. J. Cryst. Growth 311, 1696.

Shibasaki, I., Ishida, S., Geka, H., Manago, T., 2015. Low temperature transport property of the InSb and InAsSb quantum wells with $Al_{0.1}In_{0.9}Sb$ barrier layers grown by MBE. J. Cryst. Growth 425, 76–79.

Wiess, H., 1969. Structure and Application of Galvanomagnetic Devices. Pergamon Press, Oxford.

This page intentionally left blank